Journal of Materials Chemistry

Cite this: J. Mater. Chem., 2012, 22, 9522

www.rsc.org/materials

PAPER

The effect of the B-site cation and oxygen stoichiometry on the local and average crystal and magnetic structures of $Sr_2Fe_{1.9}M_{0.1}O_{5+y}$ (M = Mn, Cr, Co; y = 0, 0.5)

Farshid Ramezanipour,[ab] John E. Greedan,*[ab] Lachlan M. D. Cranswick,†[c] V. Ovidiu Garlea,[d] Joan Siewenie,[e] Graham King,[e] Anna Llobet[e] and Ronald L. Donaberger[c]

Received 16th February 2012, Accepted 12th March 2012
DOI: 10.1039/c2jm30957b

Six compounds with formula $Sr_2Fe_{1.9}M_{0.1}O_{5+y}$ (M = Mn, Cr, Co; y = 0, 0.5) were synthesized in air and argon, exhibiting surprisingly different properties depending on the B-cation type in spite of the low (5%) doping level. All argon synthesized phases, y ~ 0, have long range brownmillerite ordering of oxygen vacancies with *Icmm* symmetry as shown by neutron diffraction (ND). All show long-range G-type antiferromagnetic order with Néel temperatures, T_N, from variable temperature ND of 649(3) K, 636(2)K and 668(5)K for Cr, Mn and Co-compounds, respectively, compared with $Sr_2Fe_2O_5$, T_N = 693 K. Competing ferromagnetic interactions may be responsible for the anomalously low value in the M = Mn case. The air synthesized phases with y ~ 0.5 show surprising variation with M as investigated by X-ray, TOF and constant wavelength neutron diffractions. The M = Co compound is isostructural with $Sr_4Fe_4O_{11}$ ($Sr_2Fe_2O_{5.5}$), *Cmmm*, while the M = Cr phase is cubic, *Pm*-3*m*, and that for M = Mn appears to be cubic but the reflections are systematically broadened in a manner which suggests a local *Cmmm* structure. NPDF studies show that the local structure of the Cr phase is better described in terms of a *Cmmm* ordering of oxygen vacancies with Fe–O coordination numbers of five and six. The M = Co material shows C-type antiferromagnetic long-range magnetic order at 4 K as found for $Sr_4Fe_4O_{11}$. T_N ~ 230 K is inferred from a ZFC-FC magnetic susceptibility divergence compared with T_N = 232 K for un-doped $Sr_4Fe_4O_{11}$. The M = Cr and Mn compounds show no long-range magnetic ordering down to 4 K, but the divergence of ZFC and FC susceptibility data indicative of spin glass-like transitions occur at ~60 K and ~45 K for Cr and Mn, respectively. ND shows both diffuse and sharp Bragg magnetic reflections at positions consistent with a *Cmmm* cell for the M = Mn phase. For the M = Cr material, a very weak magnetic Bragg peak indexed as (1/2 1/2 1/2), consistent with a G-type AF order, is found at 4 K. These results rule out a spin glass-like ground state for both materials.

Introduction

The unique physical properties of perovskites make them attractive for a variety of practical applications. Therefore, gaining an understanding of the parameters that can be used to manipulate these properties is essential. The general formula for perovskites is ABO_3, where A is a large cation, usually from the alkali earth or rare earth groups, residing in the interstitial spaces between corner sharing BO_6 octahedra that form a three dimensional network. It is possible to synthesize compounds that have lower oxygen content, *i.e.*, with oxygen vacancies but which retain the perovskite structure. These oxygen vacancies may be distributed randomly throughout the structure, or they may order. One of the commonly observed ordered systems is called brownmillerite in which the vacancies order to form alternating layers of octahedra and tetrahedra. Fig. 1 compares the perovskite and brownmillerite structures.

The properties of oxygen deficient perovskites can change depending on the B site cation type. For example it has been shown that the oxygen permeation properties will be affected by Bi doping on the B-site of $BaSc_{0.1}Co_{0.9}O_{3-\delta}$. This also affects the structural stability of this compound.[1] Such effects have also been observed for $BaFeO_{3-\delta}$, where Cu or Ni doping on the B-site

[a]*Department of Chemistry, McMaster University, Hamilton, Ontario, L8S 4M1, Canada. E-mail: greedan@mcmaster.ca*
[b]*Brockhouse Institute for Materials Research, McMaster University, Hamilton, Ontario, L8S 4M, Canada*
[c]*Canadian Neutron Beam Centre, National Research Council, Chalk River Laboratories, Chalk River, Ontario, K0J 1J0, Canada*
[d]*Neutron Scattering Sciences Division, Oak Ridge National Laboratory, Oak Ridge, Tennessee 37831, USA*
[e]*Lujan Neutron Scattering Center, Los Alamos National Laboratory, Los Alamos, New Mexico 87545, USA*
† Deceased

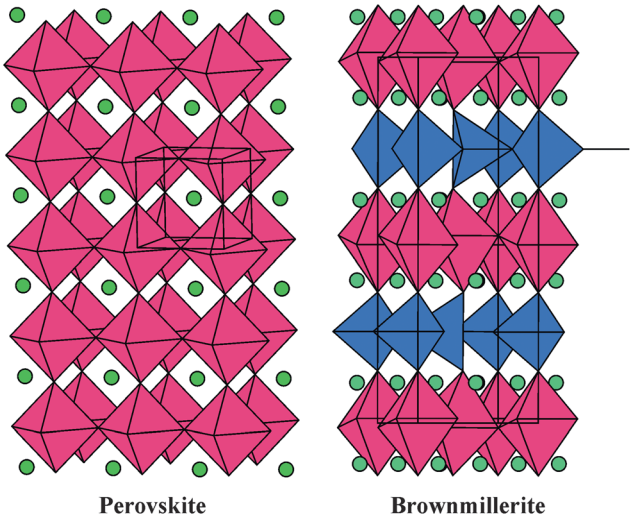

Fig. 1 A comparison between the perovskite and brownmillerite structures. The oxygen vacancies order to form alternating layers of octahedra and tetrahedra. Note the difference between the unit cell sizes. The relationship between the two is: $a_b \approx \sqrt{2}a_p$, $b_b \approx 4a_p$, $c_b \approx \sqrt{2}a_p$.

stabilizes the high temperature cubic phase even at room temperature.[2] Also, for $La_xSr_{1-x}Co_yFe_{1-y}O_{3-\delta}$, substitution of Cr^{6+} and Mg^{2+} on the B-site improves chemical and thermal stability of the system.[3] B-site cation doping is also used to explore possible cathodes for solid-oxide fuel cells.[4,5] The oxygen deficient perovskite, $Sr_2Fe_2O_{5+y}$, can adopt *Icmm*, *Cmmm*, or *I*4/*mmm* structures depending on the value of y.[6] When $y \sim 0$ a brownmillerite structure, described in *Icmm* with intact but disordered tetrahedral chains is found. For higher values, $y \sim 0.5$ and $y \sim 0.75$, structures described in *Cmmm* and *I*4/*mmm* are obtained, respectively, which involve ordered oxygen vacancies resulting in local square pyramidal and octahedral coordination of the iron atoms. The compositions of these oxidized phases are often written $Sr_4Fe_4O_{11}$($y \sim 0.5$) and $Sr_8Fe_8O_{23}$ ($y \sim 0.75$). The oxygen deficiency can be completely removed by annealing in pure oxygen, which results in a cubic perovskite structure, *Pm*-3*m*.[6]

In this article, the remarkable changes in properties of $Sr_2Fe_2O_{5+y}$ upon substitution of only 5% Fe by Cr, Mn, and Co are investigated. Six compounds, with formula $Sr_2Fe_{1.9}M_{0.1}O_{5+y}$ (M = Mn, Cr, Co) were synthesized in both argon and air and studied by powder X-ray, constant wavelength and time-of-flight

Table 1 The powder neutron refinement results at 300 K, for $Sr_2Fe_{1.9}Cr_{0.1}O_5$ synthesized in argon

$\lambda = 1.331$ and $\lambda = 2.373$, simultaneous refinement					
*Ibm*2	$a = 5.6556(4)$, $b = 15.6232(11)$, $c = 5.5320(4)$, $R_p = 0.0576$, $R_{wp} = 0.0771$				
	x	*y*	*z*	Occupancy	U_{iso} (Å^2)
Sr1	0.5121(10)	0.10994(25)	−0.0062(34)	1	0.0173(11)
Fe1	0.0629(11)	0.25	0.010(4)	1	0.0353(18)
Fe2	*0*	*0*	*0*	0.9	0.0177(13)
Cr1	*0*	*0*	*0*	0.1	0.0177(13)
O1	0.2415(24)	0.0074(4)	0.249(5)	1	0.0133(13)
O2	−0.0472(11)	0.13951(35)	−0.011(4)	1	0.0241(17)
O3	0.3544(22)	0.25	0.860(4)	1	0.0307(31)
Icmm	$a = 5.6555(4)$, $b = 15.6232(10)$, $c = 5.53172(34)$, $R_p = 0.0507$, $R_{wp} = 0.0684$				
	x	*y*	*z*	Occupancy	U_{iso} (Å^2)
Sr1	0.5111(8)	0.60984(19)	*0*	1	0.0178(9)
Fe1	0.5632(8)	0.25	0.4580(13)	0.5	0.0155(17)
Fe2	*0*	*0*	*0*	0.9	0.0163(10)
Cr1	*0*	*0*	*0*	0.1	0.0163(10)
O1	0.25	0.99254(34)	0.25	1	0.0150(10)
O2	0.0480(9)	0.13976(29)	*0*	1	0.0256(13)
O3	0.6432(17)	0.25	0.1339(18)	0.5	0.0226(24)
Time of flight neutron diffraction					
*Ibm*2	$a = 5.65913(15)$, $b = 15.6028(4)$, $c = 5.52717(14)$, $R_p = 0.0314$, $R_{wp} = 0.0446$				
	x	*y*	*z*	Occupancy	U_{iso} (Å^2)
Sr1	0.51184(26)	0.10959(7)	−0.0014(7)	1	0.00837(21)
Fe1	0.06556(29)	0.25	0.0328(6)	1	0.0165(4)
Fe2	*0*	*0*	*0*	0.932(10)	0.0109(4)
Cr1	*0*	*0*	*0*	0.068(10)	0.0109(4)
O1	0.2504(9)	0.00793(11)	0.2482(10)	1	0.00718(24)
O2	−0.04829(27)	0.14005(11)	−0.0019(9)	1	0.01586(33)
O3	0.3556(6)	0.25	0.8715(9)	1	0.0168(6)
Icmm	$a = 5.65898(14)$, $b = 15.6024(4)$, $c = 5.52714(14)$, $R_p = 0.0303$, $R_{wp} = 0.0420$				
	x	*y*	*z*	Occupancy	U_{iso} (Å^2)
Sr1	0.51093(24)	0.60957(6)	*0*	1	0.01144(21)
Fe1	0.56679(25)	0.25	0.45955(30)	0.5	0.01068(33)
Fe2	*0*	*0*	*0*	0.934(9)	0.01243(35)
Cr1	*0*	*0*	*0*	0.066(9)	0.01243(35)
O1	0.25	0.99266(11)	0.25	1	0.01124(25)
O2	0.04871(25)	0.14033(10)	*0*	1	0.01877(32)
O3	0.6423(5)	0.25	0.1280(6)	0.5	0.0127(5)

Table 2 The powder neutron refinement results at 300 K, for $Sr_2Fe_{1.9}Mn_{0.1}O_5$ synthesized in argon.

$\lambda = 1.331$ and $\lambda = 2.373$, simultaneous refinement					
*Ibm*2	$a = 5.6560(4)$, $b = 15.6318(10)$, $c = 5.5198(4)$, $R_p = 0.0536$, $R_{wp} = 0.0705$				
	x	*y*	*z*	Occupancy	U_{iso} (Å^2)
Sr1	0.5117(10)	0.11077(25)	−0.0048(34)	1	0.0199(12)
Fe1	0.0682(11)	0.25	0.015(4)	1	0.0330(17)
Fe2	*0*	*0*	*0*	0.9	0.0197(14)
Mn1	*0*	*0*	*0*	0.1	0.0197(14)
O1	0.2406(23)	0.0070(4)	0.246(5)	1	0.0159(12)
O2	−0.0492(10)	0.13937(34)	−0.007(4)	1	0.0235(16)
O3	0.3593(22)	0.25	0.865(4)	1	0.0309(30)
Icmm	$a = 5.6558(4)$, $b = 15.6313(9)$, $c = 5.51966(32)$, $R_p = 0.0479$, $R_{wp} = 0.0641$				
	x	*y*	*z*	Occupancy	U_{iso} (Å^2)
Sr1	0.5107(8)	0.61049(19)	*0*	1	0.0204(10)
Fe1	0.5685(8)	0.25	0.4574(12)	0.5	0.0132(15)
Fe2	*0*	*0*	*0*	0.9	0.0179(11)
Mn1	*0*	*0*	*0*	0.1	0.0179(11)
O1	0.25	0.99306(33)	0.25	1	0.0182(11)
O2	0.0498(9)	0.13977(28)	*0*	1	0.0254(13)
O3	0.6401(17)	0.25	0.1290(18)	0.5	0.0245(25)
Time of flight neutron diffraction					
*Ibm*2	$a = 5.65222(23)$, $b = 15.6313(6)$, $c = 5.51648(22)$, $R_p = 0.0357$, $R_{wp} = 0.0473$				
	x	*y*	*z*	Occupancy	U_{iso} (Å^2)
Sr1	0.5119(4)	0.11015(10)	−0.0041(11)	1	0.01103(32)
Fe1	0.0674(4)	0.25	0.0271(11)	1	0.0233(6)
Fe2	*0*	*0*	*0*	0.931(6)	0.0153(6)
Mn1	*0*	*0*	*0*	0.069(6)	0.0153(6)
O1	0.2497(13)	0.00715(17)	0.2482(16)	1	0.0110(4)
O2	−0.0483(4)	0.13965(15)	−0.0021(15)	1	0.0186(5)
O3	0.3575(8)	0.25	0.8733(14)	1	0.0184(9)
Icmm	$a = 5.65223(20)$, $b = 15.6305(5)$, $c = 5.51650(20)$, $R_p = 0.0319$, $R_{wp} = 0.0425$				
	x	*y*	*z*	Occupancy	U_{iso} (Å^2)
Sr1	0.51174(29)	0.60996(7)	*0*	1	0.01237(27)
Fe1	0.56904(31)	0.25	0.4586(4)	0.5	0.0100(4)
Fe2	*0*	*0*	*0*	0.924(5)	0.0138(5)
Mn1	*0*	*0*	*0*	0.076(5)	0.0138(5)
O1	0.25	0.99304(14)	0.25	1	0.01238(32)
O2	0.04802(32)	0.14007(12)	*0*	1	0.0195(4)
O3	0.6398(6)	0.25	0.1253(7)	0.5	0.0110(6)

(TOF) neutron diffraction, as well as SQUID magnetometry. Neutron Pair Distribution function analyses were also used to study the local structures of these materials.

Experimental

Synthesis

Three $Sr_2Fe_{1.9}M_{0.1}O_{5+y}$ compounds, with M= Cr, Mn and Co, were synthesized in air using stoichiometric amounts of $SrCO_3$ (99.9% Sigma Aldrich), Fe_2O_3 (99.998% Alfa Aesar), Mn_2O_3 (99.9% Cerac), Cr_2O_3 (99.97% Alfa Aesar), and Co_3O_4 (99.3% Fisher Scientific), ground and pressed into pellets. In all cases the syntheses were performed at 1250 °C, with both heating and cooling rates of 100 °C h^{-1}. Several intermediate regrinding and refiring steps were performed until pure phases were obtained. The syntheses were also performed in argon atmosphere, under the same conditions for all three M = Cr, Mn and Co.

X-ray and Neutron diffraction

Powder X-ray diffraction data were obtained on a PANalytical X'Pert Pro MPD diffractometer with a linear X'Celerator detector. In all cases Cu-Kα_1 radiation ($\lambda = 1.54056$ Å) with 2θ step interval 0.0084° was used for data collection.

Constant wavelength powder neutron diffraction data were obtained on the C2 diffractometer at the Canadian Neutron Beam Centre at Chalk River, Ontario and the HB2A diffractometer, at the High Flux Isotope Reactor at the Oak Ridge National Lab. The C2 data were collected at a variety of temperatures from 4 K to 700 K. A wavelength of 2.373 Å was used to collect data within the 2θ range of 4.4° to 84.5° at all temperatures. A wavelength of 1.331 Å was also used at 4 K and 300 K to obtain data from 34.9° to 115.0°. In both cases the 2θ step size was 0.10°.

HB2A measurements were performed using an incident neutron wavelength of 2.41 Å, selected from the (113) plane of a vertically focusing Ge monochromator. A pyrolytic graphite (PG) filter was used to remove the higher order contamination of the beam. A 12′ Soller slit collimator was used in front of the monochromator and 21′ in front of the sample. The scattered neutrons were detected by an array of 44 equally spaced (~2.7°) ^{3}He detectors; each proceeded by a 6′ mylar foil collimator. For the data collection, the detector array was scanned to cover the total 2θ range of 10.5° to 131.9°, in steps of 0.1°. More details

Table 3 The powder neutron refinement results at 300 K, for $Sr_2Fe_{1.9}Co_{0.1}O_5$ synthesized in argon

$\lambda = 1.331$ and $\lambda = 2.373$, simultaneous refinement					
*Ibm*2	$a = 5.6859(4)$, $b = 15.6604(10)$, $c = 5.5410(4)$, $R_p = 0.0603$, $R_{wp} = 0.0788$				
	x	*y*	*z*	Occupancy	U_{iso} (Å^2)
Sr1	0.5154(9)	0.10946(31)	−0.0007(31)	1	0.0079(16)
Fe1	0.0669(10)	0.25	0.0242(11)	1	0.0167(23)
Fe2	0	0	0	0.9	0.0094(17)
Co1	0	0	0	0.1	0.0094(17)
O1	0.2363(16)	0.0081(4)	0.2391(32)	1	−0.0015(18)
O2	−0.0481(11)	0.1410(5)	−0.0105(31)	1	0.0124(18)
O3	0.3605(24)	0.25	0.8751(30)	1	0.0192(31)
Icmm	$a = 5.68161(34)$, $b = 15.6489(9)$, $c = 5.53692(32)$, $R_p = 0.0547$, $R_{wp} = 0.0723$				
	x	*y*	*z*	Occupancy	U_{iso} (Å^2)
Sr1	0.5142(8)	0.60939(26)	0	1	0.0079(14)
Fe1	0.5685(8)	0.25	0.4562(11)	0.5	0.0029(20)
Fe2	0	0	0	0.9	0.0061(14)
Co1	0	0	0	0.1	0.0061(14)
O1	0.25	0.9919(4)	0.25	1	0.0064(14)
O2	0.0489(9)	0.1411(4)	0	1	0.0149(15)
O3	0.6396(19)	0.25	0.1246(21)	0.5	0.0087(24)
Time of flight neutron diffraction					
*Ibm*2	$a = 5.66145(17)$, $b = 15.5960(5)$, $c = 5.51749(17)$, $R_p = 0.0318$, $R_{wp} = 0.0441$				
	x	*y*	*z*	Occupancy	U_{iso} (Å^2)
Sr1	0.51312(26)	0.10946(9)	−0.0035(7)	1	0.00988(24)
Fe1	0.06839(29)	0.25	0.0345(7)	1	0.0172(4)
Fe2	0	0	0	0.9	0.00885(26)
Co1	0	0	0	0.1	0.00885(26)
O1	0.2509(9)	0.00724(14)	0.2482(10)	1	0.00903(27)
O2	−0.04826(27)	0.14116(13)	−0.0054(10)	1	0.01543(35)
O3	0.3563(6)	0.25	0.8769(9)	1	0.0146(6)
Icmm	$a = 5.66160(15)$, $b = 15.5963(4)$, $c = 5.51770(15)$, $R_p = 0.0274$, $R_{wp} = 0.0388$				
	x	*y*	*z*	Occupancy	U_{iso} (Å^2)
Sr1	0.51265(22)	0.60915(7)	0	1	0.01164(20)
Fe1	0.56889(22)	0.25	0.45654(26)	0.5	0.00746(29)
Fe2	0	0	0	0.9	0.00857(20)
Co1	0	0	0	0.1	0.00857(20)
O1	0.25	0.99258(11)	0.25	1	0.01030(23)
O2	0.04840(23)	0.14082(10)	0	1	0.01675(28)
O3	0.6401(5)	0.25	0.1237(5)	0.5	0.0096(4)

about the HB2A instrument and data collection strategies can be found in reference.[7] Powder samples weighting about 3 g were placed in vanadium cans (8 mm i.d. by 5 cm) and loaded in a Janis top-loading CCR capable of achieving temperatures up to 700 K.

Time of flight neutron powder diffraction data were collected on the instrument NPDF at the M. Lujan Jr. Center for Neutron Scattering at the Los Alamos Neutron Science Center.[8] Four data banks were collected at detector angle of 45° (bank 1), 90° (bank 2), 119° (bank 3) and 148° (bank 4).

Magnetic property measurements

Bulk magnetization measurements were performed using a Quantum Design MPMS SQUID Magnetometer. The field sweep, as well as zero-field cooled and field cooled (ZFC/FC) magnetic susceptibility measurements from 5 K to 300 K were performed on powder samples in gelatin capsules. Quartz sample-holders were used for the susceptibility measurements from 300 K to 700 K.

Thermal gravimetric analysis (TGA)

The TGA experiments were performed on a Netzsch STA-409 TGA-DTA instrument (Thermal Gravimetric Analyzer-Differential Thermal analyzer), by heating the argon synthesized samples in air at the rate of 5 °C min^{-1}, up to 1250 °C, and measuring the weight gains.

Results and discussion

Crystal structures of compounds synthesized in argon, y ~ 0

Powder X-ray and neutron diffraction data were used for structural characterizations. The GSAS program,[9] using the EXPGUI interface[10] was employed for the Rietveld refinements. The argon synthesized compounds are all brownmillerites with long-range ordering of oxygen vacancies (Fig. 1). There are four space groups reported for brownmillerites which depend on the relative orientations of the tetrahedral chains which can exist in either R or L handedness within and between the chain layers.[11,12] If the intra/inter planar relationship is RR (or LL), the polar space group *I*2*mb* (*Ibm*2) is found (the chains possess an

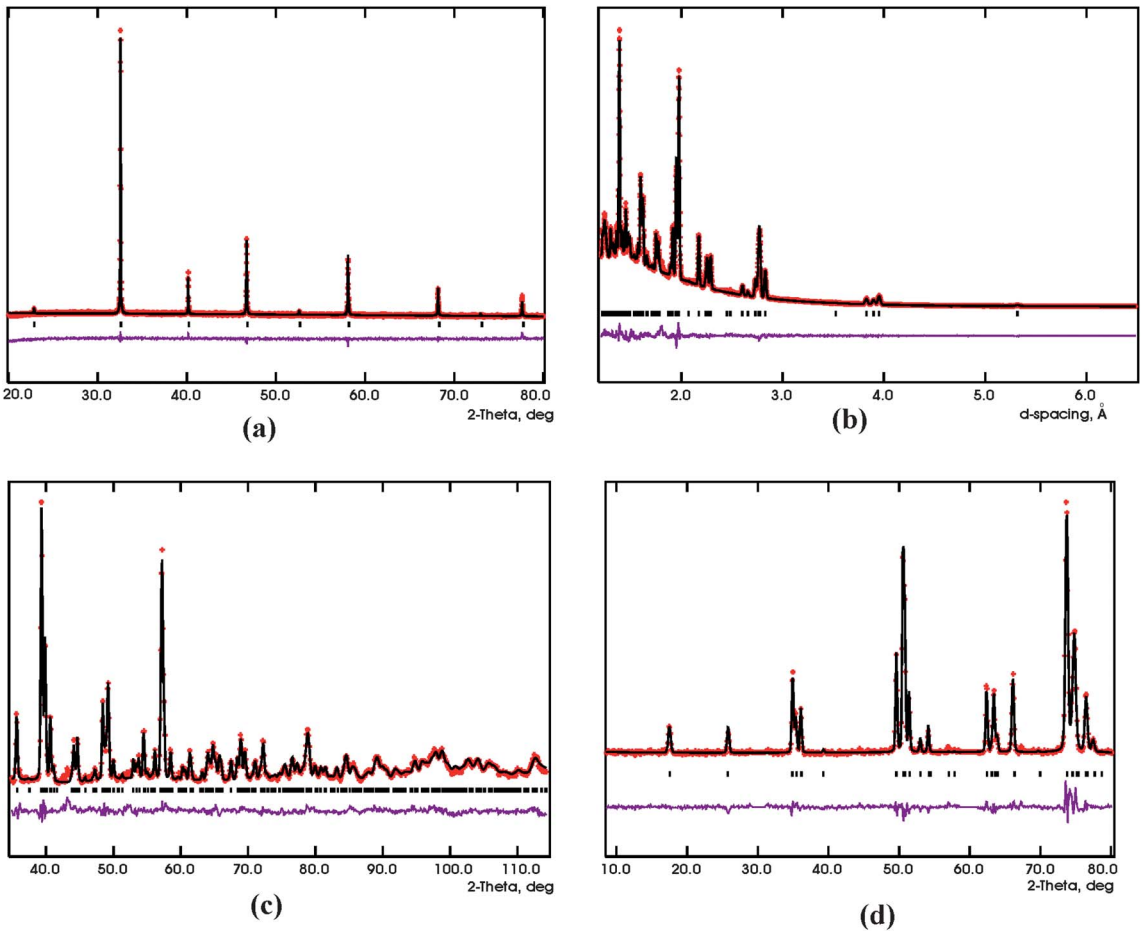

Fig. 2 Rietveld refinement profiles for $Sr_2Fe_{1.9}Co_{0.1}O_5$ (*Icmm*) synthesized in argon. Very similar refinement profiles were also obtained for the Mn and Co compounds. **(a)** Powder X-ray diffraction with $\lambda = 1.54056$ Å. **(b)** Time-of-Flight neutron diffraction. Only one of the four banks is shown. The detector angle for this bank was 45°. **(c)** and **(d)** Constant wavelength powder neutron diffraction, $\lambda = 1.3307$ Å and $\lambda = 2.3730$ Å, respectively. The stars indicate the experimental data, the solid line shows the model, the vertical tick marks locate Bragg peak positions and the lower solid line is the difference plot.

electric dipole moment). If the orientation is the same within each tetrahedral layer but alternates from one layer to the next (RL or LR) the non-polar *Pnma* occurs. A structure with long-range disorder of tetrahedral chain orientation is described by *Imma* (*Icmm*). Finally, there is a much less common space group *Pcmb* (*Pbcm*) that describes an alternating orientation of tetrahedral chains within and between adjacent tetrahedral layers (RL/LR).[11,12] Different settings of these space groups have been used by different authors, but the above notations refer to a cell with $b > c > a$, and the ones in brackets are the other commonly used settings. The *Pcmb* systems can be easily recognized by the presence of supercell reflections due to a doubling of one axis. In addition, the primitive cells can be readily identified by the occurrence of (1 5 1) and (1 3 1) reflections that are not allowed in I-centering. These reflections are absent for all $Sr_2Fe_{1.9}M_{0.1}O_5$ (M = Cr, Mn,Co) compounds. The *Ibm*2 and *Icmm* models were therefore refined. The refinements yield good fits for both models using X-ray, as well as constant wavelength and time of flight neutron diffraction data. This is generally expected, as it is usually difficult to distinguish these two space groups using powder data. However, the *Icmm* model results in better agreement factors and more uniform thermal displacement parameters throughout the structure. It should be noted that there are actually fewer degrees of freedom for atomic positions in *Icmm*, and therefore, fewer parameters to be refined. In addition, the TOF data in all cases resulted in better fits due to the significantly larger Q range obtained from TOF experiments. Tables 1–3 show the refinement results for both *Icmm* and *Ibm*2 models using constant wavelength and TOF neutron data. Fig. 2 shows the refinement profiles for the Cr-compound. Based on the crystal field stabilization energy, Cr^{3+} ($3d^3$: t_{2g}^3) and Mn^{3+} ($3d^4$: $t_{2g}^3e_g^1$) are expected to prefer the octahedral site. In the case of Mn and Cr, the octahedral site preference has been shown for Ca_2FeMnO_5[13] and $Ca_2Fe_{1.5}Cr_{0.5}O_5$.[14] Rietveld refinements showed that for all three phases (Cr, Mn and Co), more reasonable thermal displacement parameters were obtained when they were placed on the octahedral site. Therefore, the final refinements were performed with Cr, Mn and Co on the octahedral site.

In all three brownmillerite compounds, elongation of octahedra is observed (Table 4). The two Fe–O2 bonds are longer than the other four bonds. O2 is the oxygen that links octahedral and tetrahedral layers. For the tetrahedra, the Fe–O2 bonds are shorter than the other two bonds. Therefore, O2 forms longer bonds with

Table 4 Selected bond distances (Å) and angles (°) for brownmillerite compounds, *Icmm*, from time-of-flight neutron diffraction refinements

$Sr_2Fe_{1.9}Cr_{0.1}O_5$	
Fe1–O2	1.8483(16) × 2
Fe1–O3	1.882(4)
Fe1–O3	1.8911(33)
Fe2–O1	1.98089(10) × 4
Fe2–O2	2.2067(15) × 2
O2–Fe1–O2	136.03(12)
O2–Fe1–O3	101.45(6)
O2–Fe1–O3	104.40(7)
O3–Fe1–O3	106.36(11)
O1– Fe2–O1	88.462(6)
O1– Fe2–O1	91.538(6)
O1– Fe2–O2	88.17(5)
O1– Fe2–O2	91.83(5)
$Sr_2Fe_{1.9}Mn_{0.1}O_5$	
Fe1–O2	1.8553(20) × 2
Fe1–O3	1.882(4)
Fe1–O3	1.885(4)
Fe2–O1	1.97751(13) × 4
Fe2–O2	2.2062(19) × 2
O2–Fe1–O2	135.67(15)
O2–Fe1–O3	101.30(7)
O2–Fe1–O3	104.56(8)
O3–Fe1–O3	106.92(13)
O1–Fe2–O1	88.438(7)
O1–Fe2–O1	91.562(7)
O1–Fe2–O2	88.09 (7)
O1– Fe2–O2	91.91 (7)
$Sr_2Fe_{1.9}Co_{0.1}O_5$	
Fe1–O2	1.8434(17) × 2
Fe1–O3	1.8805(32)
Fe1–O3	1.8880(29)
Fe2–O1	1.97979(11) × 4
Fe2–O2	2.2132(16) × 2
O2–Fe1–O2	134.96(11)
O2–Fe1–O3	101.79(5)
O2–Fe1–O3	104.53(6)
O3–Fe1–O3	106.85(10)
O1–Fe2–O1	88.334(6)
O1–Fe2–O1	91.666(6)
O1–Fe2–O2	88.25(6)
O1– Fe2–O2	91.75(6)

the octahedral Fe and shorter bonds with tetrahedral Fe. There is a strong distortion in the tetrahedral layer, where some tetrahedral angles deviate from the ideal, 109.5°, by more than 26.5°. There is a smaller degree of distortion in the octahedral layer, where the deviations from ideal angles are less than 2° (Table 4).

Crystal structures of compounds synthesized in air, y ~ 0.5

The air synthesized Co-compound, $Sr_2Fe_{1.9}Co_{0.1}O_{5+y}$, has an orthorhombic *Cmmm* symmetry, as confirmed by X-ray, TOF and constant wavelength neutron diffraction refinements (Fig. 3 and Table 5). The refinement of oxygen occupancies using the neutron data resulted in very small deviations from full occupancy. Therefore, they were fixed at 1, consistent with y = 0.5. This is also consistent with the result of the thermogravimetric analysis based on the fact that all three air synthesized compounds can be converted to the vacancy-ordered brownmillerites, by firing in argon resulting in the loss of oxygen. The reverse process is also possible. Based on these analyses, and assuming y ~ 0 for the brownmillerite obtained upon firing in argon, y = 0.52 was obtained for the *Cmmm* compound. This compound exhibits vacancy ordering (Fig. 4), which results in dimeric units of square pyramids and chains of octahedrally coordinated Fe atoms. This is the same structure found for $Sr_4Fe_4O_{11}$ ($Sr_2Fe_2O_{5.5}$) which is not surprising. Each pyramid shares the four corners of its base with four octahedra, such that the dimeric units are isolated from each other and there is no corner-sharing between them. The chains of octahedra are also isolated from each other by square pyramidal dimers (Fig. 4). Viewing the individual pyramids along the *a*-axis, an alternating up and down orientation pattern is evident. Also, taking the square pyramidal sub-lattice alone in Fig. 4a, it can be seen that oxygen atoms and vacancies alternate along both *a* and *b*-axes, forming isolated dimers that are shifted parallel to *b* relative to the dimers on their right and left.

In sharp contrast, for air synthesized $Sr_2Fe_{1.9}M_{0.1}O_{5+y}$ (M = Cr and Mn), a cubic cell was readily identified from the X-ray diffraction pattern. However, closer inspection of the data disclosed a significant difference between the M = Cr and Mn materials. Fig. 5a displays the X-ray peak widths as a function of scattering angle for both phases. Note that while the behavior for the M = Cr compound shows a smooth increase with increasing 2θ, such as might be expected from the resolution function of the diffractometer, that for the M = Mn analog shows a highly irregular variation which depends strongly upon the Miller indices of the individual reflections. A similar but much less marked trend was noticed in the neutron diffraction data due to the inherent lower resolution. In Fig. 5b, the corresponding X-ray pattern for *Cmmm* $Sr_2Fe_{1.9}Co_{0.1}O_{5+y}$ is indexed as pseudo-cubic. Note the correspondence between the broadened "cubic" reflections such as (200) and (310) in the M = Mn phase and the strong splittings evident in the M = Co phase. Three samples of the M = Mn phase were prepared and the results were variable but similar to those of Fig. 5a. In one case, a clear core/shell structure was evident upon comparison of X-ray data, which are more sensitive to the surface and showed a cubic pattern, with-neutron data which probe the bulk and disclosed a mixed *Pm*-3*m*/*Cmmm* pattern. It seems clear that under these conditions of synthesis, the M = Mn material is not fully converted to a *Pm*-3*m* structure but retains at least a short range order related to that of the *Cmmm* phase, whereas the M = Cr is indeed *Pm*-3*m*. A *Pm*-3*m* model (Table 6) for M = Cr was found to be in excellent agreement with both X-ray and neutron diffraction results. Fig. 6 shows the Rietveld refinement profiles for the Cr-compound. Refinements of oxygen site occupancy gives y ~ 0.568(8) for this material (Table 6). Remarkably, the neutron data for the M = Mn phase could also be analyzed reasonably well with the *Pm*-3*m* model and parallel results are included in Table 6, but given the preceding discussion, these should be regarded with caution.

Thermogravimetric analyses were also performed and resulted in y = 0.66(8) for the disordered *Pm*-3*m* materials Cr and Mn-compounds, respectively, within experimental error of the values deduced from the neutron data.

As mentioned before, the *Pm*-3*m* and *Cmmm*, structures occur for $Sr_2Fe_2O_{5+y}$. The *Pm*-3*m* structure corresponds to y ~ 1 and is

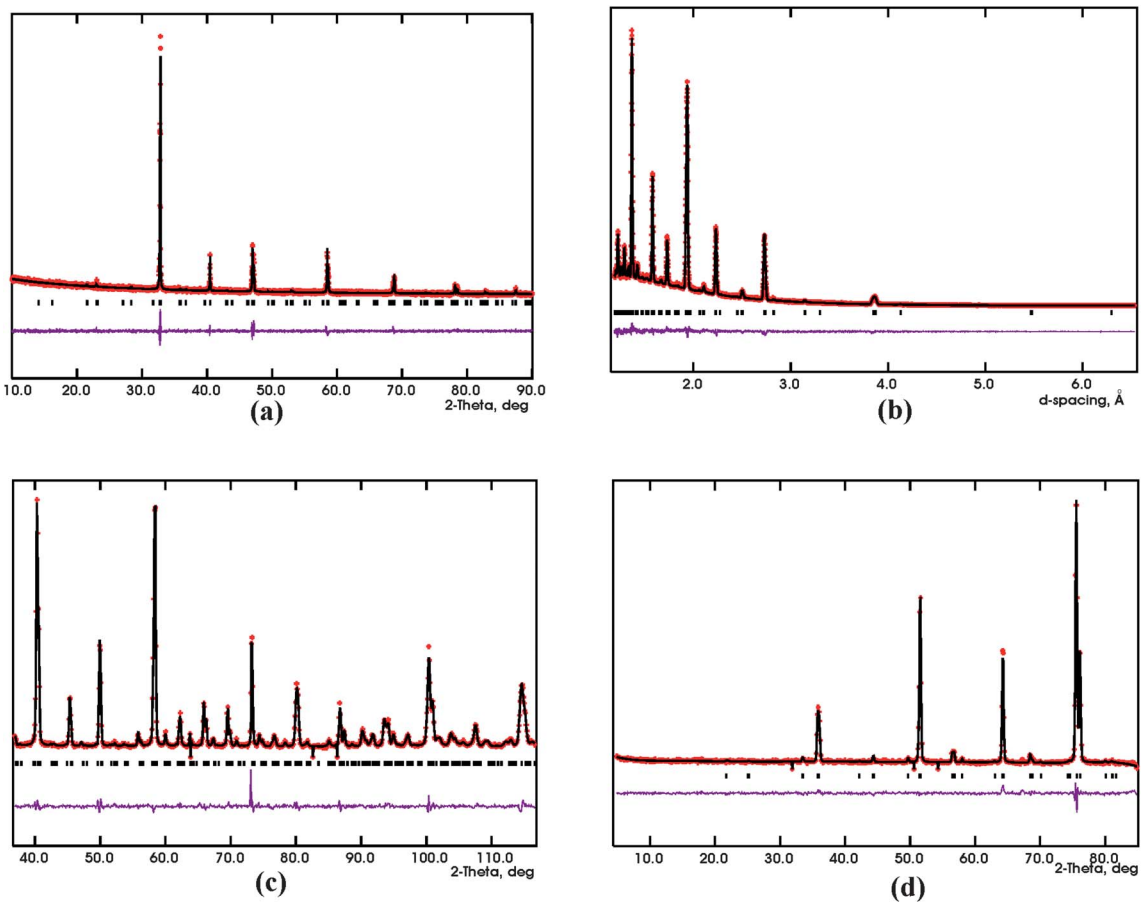

Fig. 3 Rietveld refinement profiles for $Sr_2Fe_{1.9}Co_{0.1}O_{5+y}$ (*Cmmm*) synthesized in air. **(a)** Powder X-ray diffraction with $\lambda = 1.54056$ Å. (b) Time-of-flight neutron diffraction. Only one of the four banks is shown. The detector angle for this bank was 45°. **(c)** and **(d)** Constant wavelength powder neutron diffraction $\lambda = 1.3307$ Å and $\lambda = 2.3730$ Å, respectively. The stars indicate the experimental data, the solid line shows the model, the vertical tick marks locate Bragg peak positions and the lower solid line is the difference plot.

only obtained by firing the sample in pure oxygen,[6] while *Cmmm* is obtained for y = 0.5 by adjusting the oxygen content using proper mixture of gases.[6] At this point, it is not clear how substitution of 5% Cr destroys the ordering of vacancies leading to the disordered cubic, *Pm*-3*m*, structure. However, as discussed below, the local structures of these materials seem to be different from their average structures.

Local structures of the air synthesized phases

Neutron-Pair-Distribution-Function (NPDF) analyses were performed to study the local structures of these materials. Both Bragg peaks and diffuse scattering are taken into account equally in this method. First, corrections and normalization are made to the powder data that are acquired to very large momentum transfer, Q. A sine Fourier transform is then performed to give the atomic pair distribution, G(r). The G(r) contains peaks whose intensities depend on the product of the neutron scattering lengths of the atoms that interact at a particular distance, r, and the number of those interatomic interactions. To obtain an initial characterization of the local structure, the G(r) is compared with the inter-atomic distances expected for the average structure and others which are plausible models for the local structure. A more detailed and quantitative local structure picture is available by fitting the G(r) data to chosen crystallographic models within a specified length scale using the PDFGUI program[15] which is similar in concept to Rietveld refinement but done in direct space. A second, complementary direct spaced analysis was applied based on the reverse Monte Carlo (RMC) method using the program RMCProfile.[16] Here a large supercell is constructed and the atoms are permitted to move from the positions of the average structure providing models which are then evaluated by fitting to the observed G(r). A valuable feature of the RMC method is that so-called partial G(r) functions for individual bond pairs are extracted. These bond pair partials are then compared to expected bond length distributions for model compounds containing the relevant atoms in different oxidation states and coordination environments to provide a more detailed picture of the local structure. NPDF data are available for the M = Cr and Co materials.

Local structure for M = Cr

Air synthesized $Sr_2Fe_{1.9}Cr_{0.1}O_{5+y}$ with a *Pm*-3*m* average structure, is expected to show only one inter-atomic distance for each of the following atom pairs: Sr–O, Fe–O, Sr–Fe, and Sr–Sr.

Table 5 The time of flight neutron powder refinement results for $Sr_2Fe_{1.9}Co_{0.1}O_{5+y}$ synthesized in air

Cmmm	$a = 10.96191(24)$, $b = 7.69419(13)$, $c = 5.46764(11)$, $R_p = 0.0370$, $R_{wp} = 0.0486$				
	x	*y*	*z*	Occupancy	U_{iso} (Å^2)
Sr1	0.5	0	0.5	1	0.0041(13)
Sr2	0	0	0.5	1	0.0057(10)
Sr3	0.25667(32)	0	0	1	0.0074(10)
Fe1	0.5	0.24845(27)	0	1	0.0046(4)
Fe2	0.25	0.25	0.5	0.9	0.0037(5)
Co1	0.25	0.25	0.5	0.1	0.0037(5)
O1	0.5	0	0	1	0.0083(12)
O2	0.26468(35)	0	0.5	1	0.0078(8)
O3	0.37932(23)	0.27147(11)	0.2495(7)	1	0.01271(18)

Bond distances (Å)	
Fe1–O1	1.9116(21)
Fe1–O3	1.9086(30) × 4
Fe2–O2	1.93027(32) × 2
Fe2–O3	1.9780(29) × 4
Sr1–O1	2.73382(5) × 2
Sr1–O2	2.580(4) × 2
Sr1–O3	2.8264(27) × 8
Sr2–O2	2.901(4) × 2
Sr2–O3	2.5918(28) × 8
Sr3–O1	2.667(4)
Sr3–O2	2.73523(21) × 2
Sr3–O3	2.8341(30) × 4
Sr3–O3	2.679(4) × 4

However, examining the G(r) data at short r reveals that there are many features not accounted for by the *Pm*-3*m* model (Fig. 7a). This indicates a local ordering of oxygen vacancies. Given that the composition of this phase is close to that for $Sr_2Fe_2O_{5.5}$, a *Cmmm* local model based on Fe–O coordination numbers (CN) of 5 and 6 might be expected. As well, local brownmillerite ordering with CN of 4 and 6 cannot be ruled out, *a priori*. Both models were tested using PDFGUI profile analysis along with the fully disordered *Pm*-3*m* model. As expected, the *Pm*-3*m* model for the range of r = 1.5 Å to 5 Å, gives a poor fit with $R_w = 20.4\%$, (Fig. 7b) while for larger distances, r = 10 Å to 20 Å the agreement is quite good, $R_w = 10.5\%$ (Fig. 7c), which is to be expected as for large distances the average structure will be a good model. For r = 1.5 Å to 5 Å, the vacancy ordered *Ibm*2 and *Cmmm* models result in a significantly better agreement factors, $R_w = 10.7\%$ (Fig. 7d) for the former and 13.6% (Fig. 7e) for the latter.

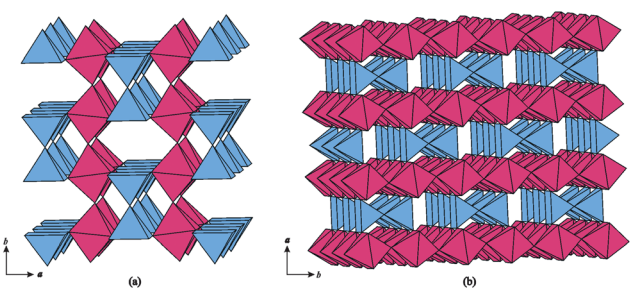

Fig. 4 Crystal structure of $Sr_2Fe_{1.9}Co_{0.1}O_{5+y}$ (*Cmmm*) synthesized in air, with ordering of oxygen vacancies resulting in chains of octahedra, separated by dimeric units of square pyramids.

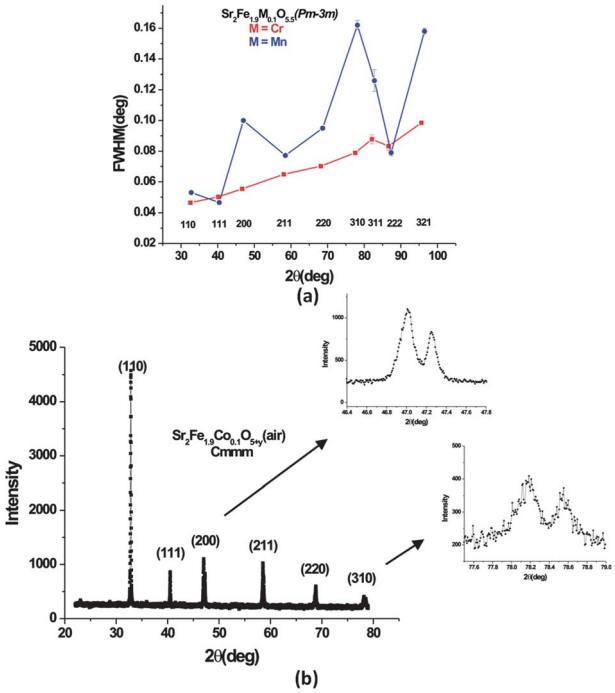

Fig. 5 **(a)** The variation of peak width *versus* scattering angle (X-ray data) and reflection index for $Sr_2Fe_{1.9}M_{0.1}O_{5+y}$ phases with M = Cr and Mn. Note the monotonic behavior for M= Cr which contrasts with that for M =Mn. **(b)** The X-ray diffraction data for *Cmmm* $Sr_2Fe_{1.9}Co_{0.1}O_{5+y}$ indexed as pseudo-cubic. Note the distinct splittings of the "(200)" and "(310)" reflections which correspond to the broadened peaks in the pattern for nominally cubic $Sr_2Fe_{1.9}Mn_{0.1}O_{5+y}$ (a).

RMC fitting was also applied to this problem in order to perhaps provide a means of deciding between the two local order models. A 14 × 14 × 14 supercell containing 12,348 atoms and

Table 6 The powder refinement results, for $Sr_2Fe_{1.9}B_{0.1}O_{5+y}$ (B = Cr, Mn) synthesized in air. The results are from simultaneous refinements with powder X-ray (λ = 1.54056 Å) and neutron diffraction data (λ = 1.331 Å and λ = 2.373 Å), at 300 K

$Sr_2Fe_{1.9}Cr_{0.1}O_{5+y}$					
Pm-3*m*	$a = 3.88896(8)$, $R_p = 0.0489$, $R_{wp} = 0.0680$				
	x	*y*	*z*	Occupancy	U_{iso} (Å^2)
Sr1	0.5	0.5	0.5	1	0.0184(4)
Fe1	0	0	0	0.95	0.01009(33)
Cr1	0	0	0	0.05	0.01009(33)
O1	0.5	0	0	0.928(4)	0.0228(4)

$Sr_2Fe_{1.9}Mn_{0.1}O_{5+y}$					
Pm-3*m*	$a = 3.86638(5)$, $R_p = 0.0507$, $R_{wp} = 0.0718$				
	x	*y*	*z*	Occupancy	U_{iso} (Å^2)
Sr1	0.5	0.5	0.5	1	0.0167(4)
Fe1	0	0	0	0.95	0.0103(4)
Mn1	0	0	0	0.05	0.0103(4)
O1	0.5	0	0	0.919(3)	0.0211(5)

Interatomic distances (Å)		
	$Sr_2Fe_{1.9}Cr_{0.1}O_{5+y}$	$Sr_2Fe_{1.9}Mn_{0.1}O_{5+y}$
Fe–O	1.94448(4) × 6	1.933190(20) × 6
Sr–O	2.74991(4) × 12	2.733940(20) × 12
Sr–Sr	3.88896(8) × 6	3.86638(5) × 6
Sr–Fe	3.36794(5) × 8	3.348380(30) × 8

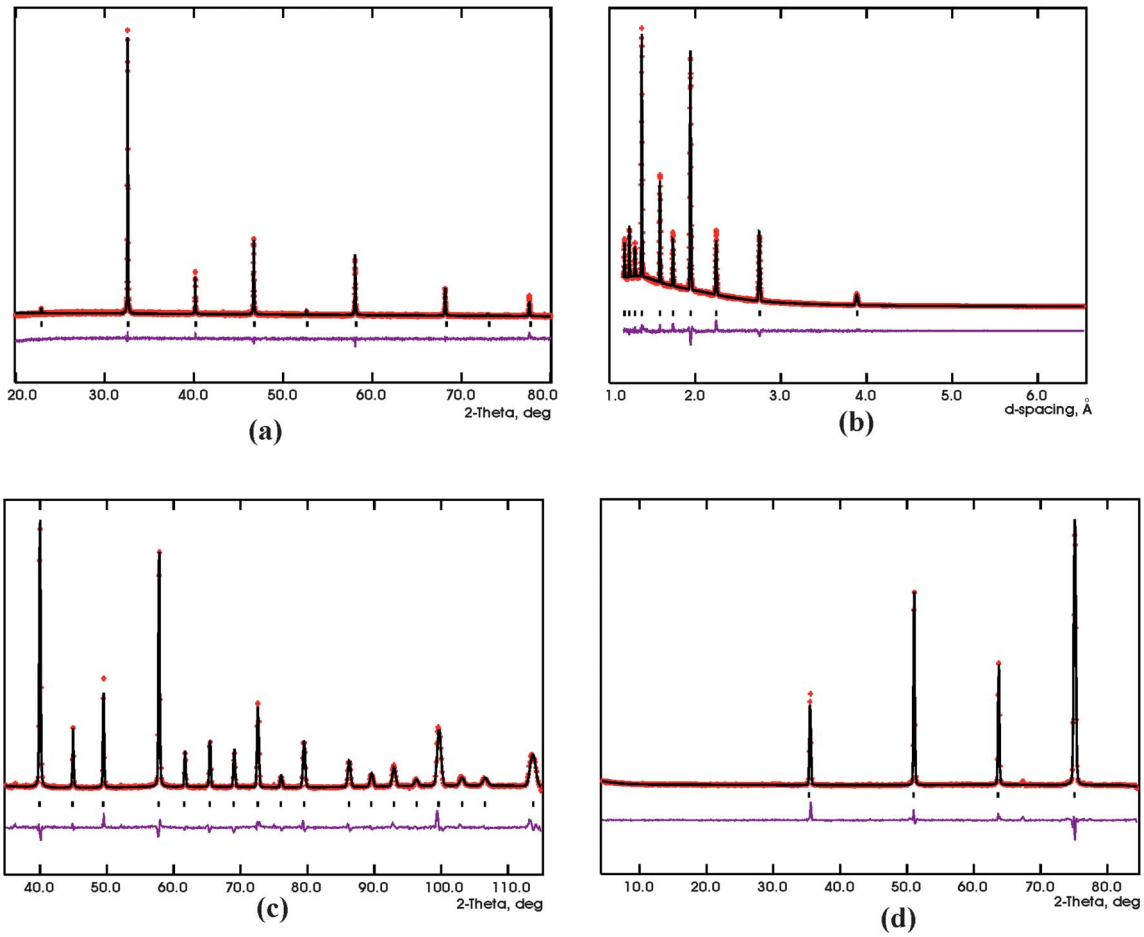

Fig. 6 Rietveld refinement profiles for $Sr_2Fe_{1.9}Cr_{0.1}O_{5+y}$ (*Pm*-3*m*) synthesized in air. **(a)** Powder X-ray diffraction with $\lambda = 1.54056$ Å. (b) Time-of-flight neutron diffraction. Only one of the four banks is shown. The detector angle for this bank was 45°. **(c)** and **(d)** Constant wavelength powder neutron diffraction $\lambda = 1.3307$ Å and $\lambda = 2.3730$ Å, respectively. The stars indicate the experimental data, the solid line shows the model, the vertical tick marks locate Bragg peak positions and the lower solid line is the difference plot. The un-indexed reflection in (d) near 67 deg is due to the vanadium sample can.

1,372 vacancy positions was generated. The positions of the atoms in the average structure were used as starting coordinates. The supercell was fit against both the G(r) and S(Q) functions to ensure that the resulting configuration was consistent with both the average long range structure and the local structure. The fit to the G(r) data is shown in Fig. 8a and the Fe–O partial G(r), Fig. 8b, is compared to expected interatomic distances determined from the two models. Note that for the brownmillerite *Icmm* model, one would expect to see a significant feature at about 2.2 Å, due to the octahedral site Fe^{3+} ion. As there is little evidence for this, and that the *Cmmm* model appears to account at least roughly for the shape of the observed Fe–O G(r), one can conclude that the latter is a better description of the local structure. This indicates that the local structure involves Fe–O coordination numbers of five and six and the presence of Fe^{3+} and Fe^{4+}. The presence of significant levels of Fe^{3+} in octahedral coordination at distances typically found in brownmillerites is ruled out.

Local structure for M = Co

The NPDF data for $Sr_2Fe_{1.9}Co_{0.1}O_{5+y}$ synthesized in air are shown in Fig. 9. Refinement of the G(r) data out to 20 Å using PDFGUI showed that the local and average structures are the same for this phase, giving $R_w = 9.59\%$.

Magnetic properties of the argon synthesized compounds

For all three brownmillerite compounds, neutron diffraction results show the presence of long range magnetic ordering at 4 K, evident from the magnetic Bragg peaks. Neutron diffraction experiments at temperatures up to 700 K were then performed to determine the magnetic structure and magnetic moments as function of temperature and to determine the magnetic transition temperatures. (Fig. 10 and 11). For all three materials, the familiar G-type structure is found in which all nearest neighbor spins are aligned antiferromagnetically. As this nomenclature was originally applied to perovskite materials, some confusion can arise in the case of brownmillerites. Recall that brownmillerites have alternating layers of octahedra and tetrahedra. If the octahedral sublattice is examined independently in Fig. 11, it is clear that the moment on each site is aligned opposite to the nearest neighbors within the same layer, but parallel to the nearest neighbors in the adjacent layers. This is a C-type antiferromagnetic arrangement, which is also found for the tetrahedral sublattice. If both octahedral and tetrahedral sublattices

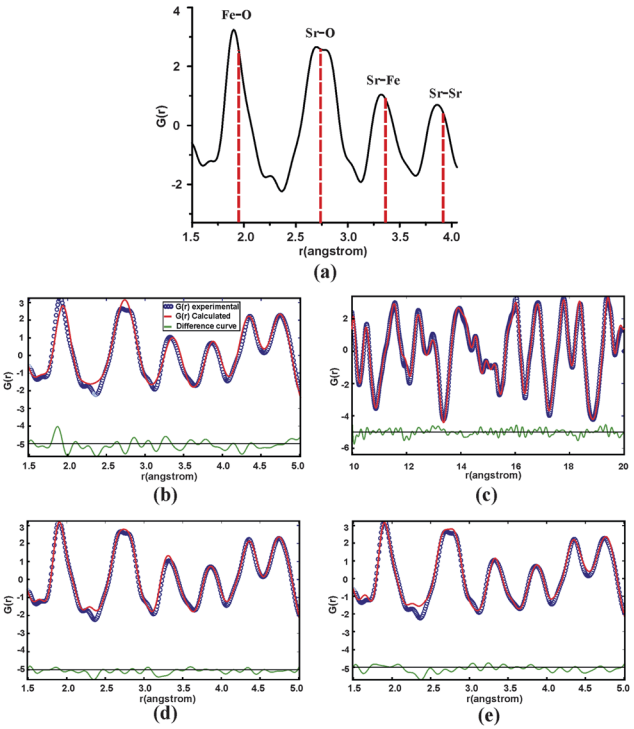

Fig. 7 NPDF data truncated at $Q_{max} = 35$ Å^{-1} for $Sr_2Fe_{1.9}Cr_{0.1}O_{5+y}$, synthesized in air, that has a cubic average structure, *Pm*-3*m*. **(a)** The match between G(r) and inter-atomic distances expected for the average structure. **(b)** PDFGUI refinement profile from r = 1.5 Å to 5 Å with a cubic *Pm*-3*m* model, $R_w = 20.4\%$. **(c)** PDFGUI refinement profile from r = 10 Å to 20 Å with a cubic *Pm*-3*m* model, $R_w = 10.5\%$ **(d)** PDFGUI refinement profile from r = 1.5 Å to 5 Å with a brownmillerite *Ibm*2 model, $R_w = 10.7\%$. **(e)** PDFGUI refinement profile from r = 1.5 Å to 5 Å with a *Cmmm* model, $R_w = 13.6\%$.

are taken together, then the overall magnetic structure can be called G-type antiferromagnetic, where the magnetic moment on each cation is oriented antiparallel to all nearest neighbor moments.

The preferred orientation of moments is along the shortest unit cell axis, *c*. This is immediately evident from the neutron diffraction patterns, as the intensity ratio of the two major magnetic peaks, marked by arrows in Fig. 10, is indicative of the magnetic moment orientation.[11] If this ratio is close to ~1, then the moments are aligned along the longest axis, and if the ratio is close to ~3, the moments are oriented parallel to the shortest axis. In this case, the ratios of the two major magnetic peaks at 4 K are 2.76, 2.41 and 2.61 for M = Cr, Mn and Co compounds, respectively.

Magnetic moments on the tetrahedral and octahedral sites were refined at different temperatures using the FullProf program suite,[17,18] and WinPLOTR.[18,19] The variations of magnetic moments with temperature are shown in Fig. 12, 13 and 14. Néel temperatures were estimated by comparing data near the transition to the equation $I(T)^{1/2} = I(4\ K)^{1/2}((T_N - T)/T_N)^{0.35}$ calculated for several temperatures near the assumed T_N. This function is valid in the so-called critical regime and the exponent is an average for the three dimensional Ising, XY and Heisenberg models.[20] For all cases there were at least two data points within the critical range and various T_N values were tried and those giving best agreement with the data were chosen. A typical comparison is shown in the inset to Fig. 12. The magnetic transition temperatures, T_N, with the estimated uncertainties are 650(2)K, 633(2)K, and 663(2)K for the Cr, Mn and Co compounds, respectively.

To analyze these results the assumption was made that for an isostructural series with constant exchange parameters, $T_N \sim \langle S \rangle^2$ where $\langle S \rangle^2$ is the average spin quantum number for the B-site ion combination. The S value for Fe^{3+} is 5/2, Co^{3+} and Mn^{3+} are both S = 2 (assuming the high spin state for Co), while Cr^{3+} is an S = 3/2 ion. The parent phase, $Sr_2Fe_2O_5$ has $T_N = 693$ K.[21] Thus, $T_N/693$ K should vary as $\langle S \rangle^2/6.25$ for each B-site composition giving expected ratios of 0.98, 0.98 and 0.96 for M = Co, Mn and Cr, respectively. The actual values are 0.96, 0.91 and 0.94 for the same three ions. While the ratios for M = Co and Cr are in reasonable agreement with expectation, the M = Mn value is clearly too low. Among the possible explanations is that Mn^{3+}–O–Fe^{3+} superexchange contributes ferromagnetic interactions which would weaken the overall antiferromagnetic exchange in disproportion to the Mn^{3+} concentration. This is in crude accord with the Goodenough-Kanamori rules for the 180° σ superexchange pathway.[22,23] It is also not impossible that a local

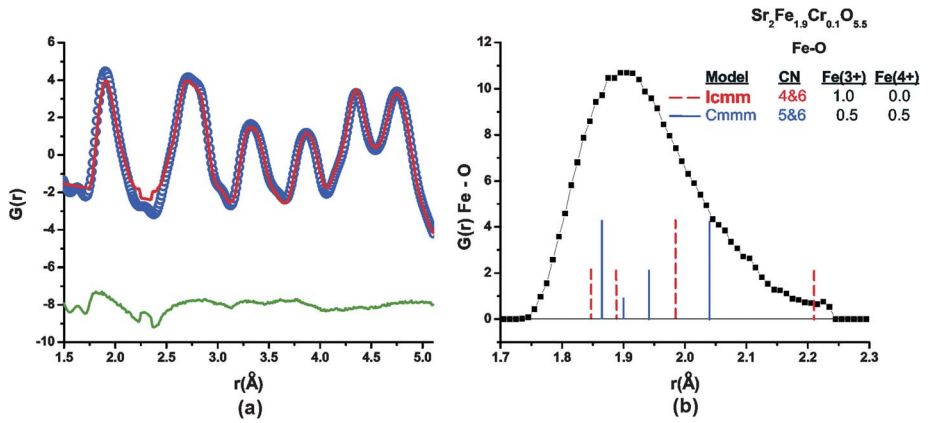

Fig. 8 **(a)** RMC fitting of the short distance G(r) for $Sr_2Fe_{1.9}Cr_{0.1}O_{5.5}$. **(b)** Comparison of the Fe–O partial G(r) over the range 1.7–2.3 Å with expected interatomic distances for model compounds. The height of each tick mark is a relative measure of the number of atom pairs at that distance.

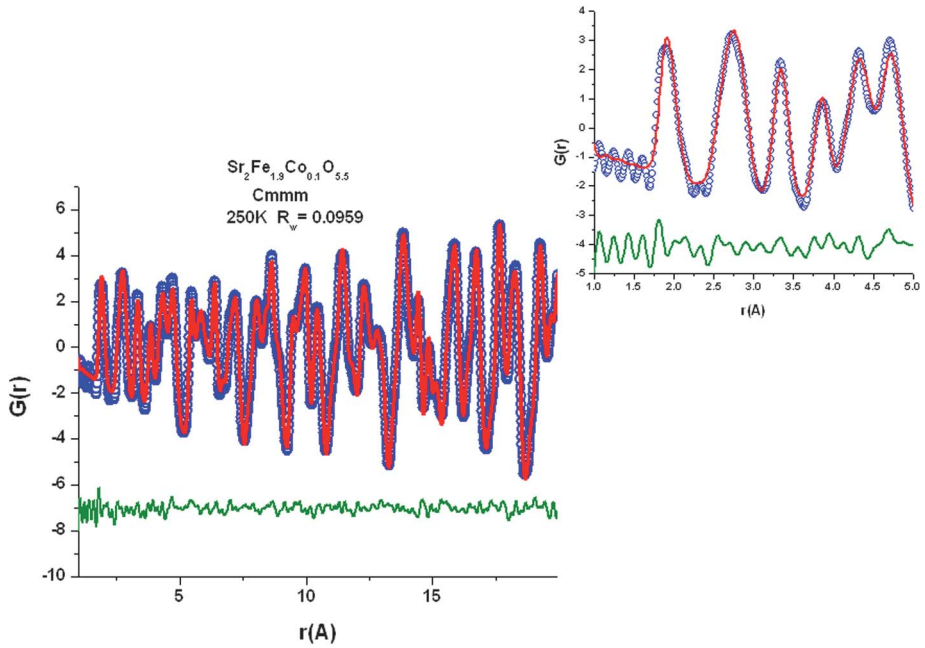

Fig. 9 Long and short (inset) range G(r) obtained from S(Q) data truncated at $Q_{max} = 35$ Å^{-1} for $Sr_2Fe_{1.9}Co_{0.1}O_{5+y}$ (air), refined with a *Cmmm* average structure. These results show that the local and average structures are the same for this material.

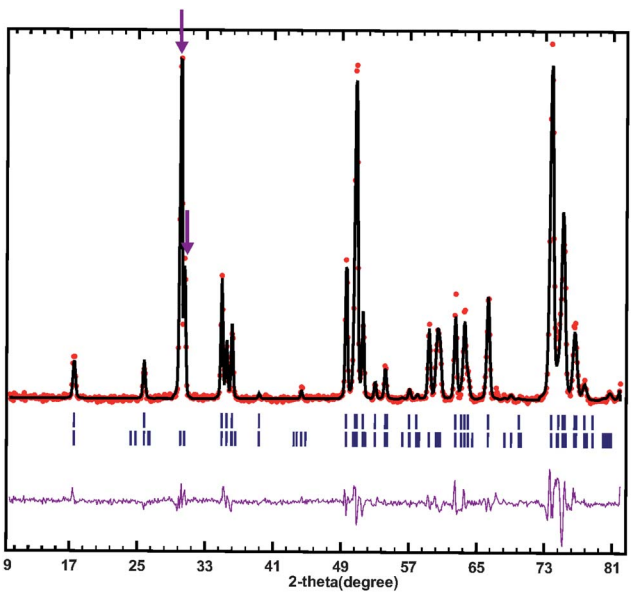

Fig. 10 The refinement profile for crystal and magnetic structures of $Sr_2Fe_{1.9}Cr_{0.1}O_5$, *Icmm*, synthesized in argon. Very similar refinement profiles were also obtained for the Mn and Co compounds. The two major magnetic peaks are shown by arrows. The magnetic structure is a G-type antiferromagnetic (Fig. 11), with magnetic moments oriented along the shortest axis, *c*. In the figure above, the circles represent the experimental data and the solid black line the model. Vertical tick marks show the positions of the peaks corresponding to the crystal (upper tick marks) and magnetic structures (lower tick marks). The purple solid line at the bottom is the difference plot. The un-indexed peak at about 68 deg is due to the vanadium sample can.

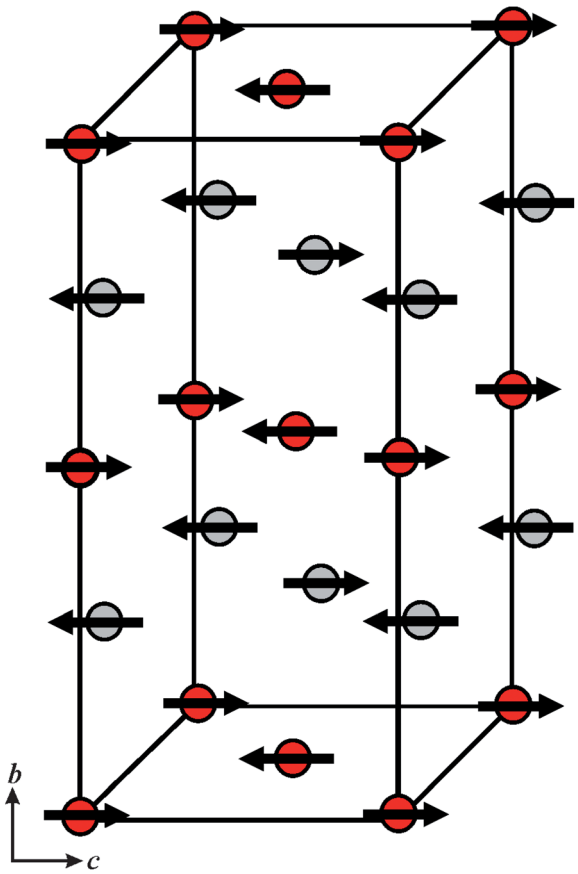

Fig. 11 The magnetic structure of $Sr_2Fe_{1.9}M_{0.1}O_5$ (M = Cr, Mn, Co), *Icmm*, synthesized in argon, at 4 K. The magnetic moment on each site is oriented anti-parallel to all nearest neighbors; a G-type antiferromagnetic structure with moments oriented along the shortest axis, *c*. Red and grey circles show octahedral and tetrahedral sites, respectively.

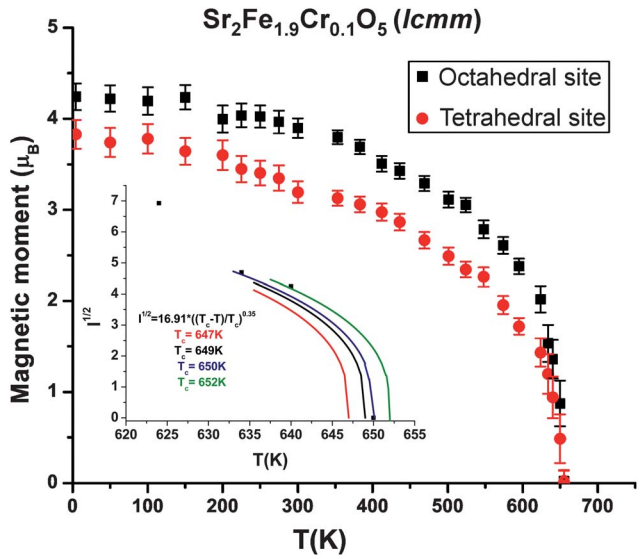

Fig. 12 The magnetic moments of $Sr_2Fe_{1.9}Cr_{0.1}O_5$, *Icmm*, synthesized in argon, as function of temperature. The magnetic transition temperature $T_N = 650(2)$ K as determined by the method described in the text and illustrated in the inset.

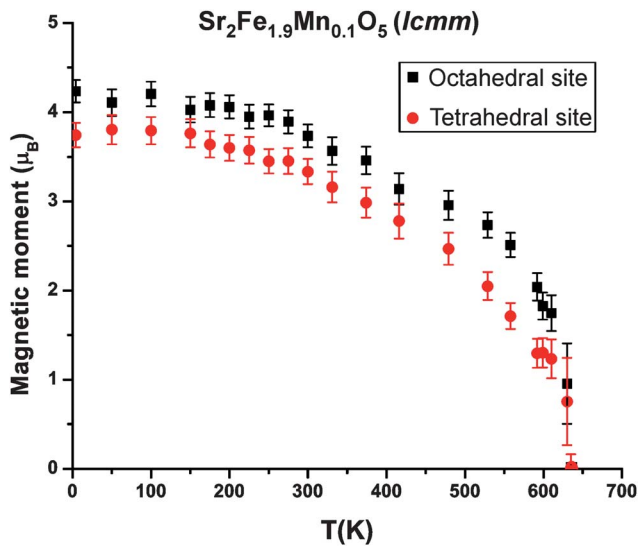

Fig. 13 The magnetic moments of $Sr_2Fe_{1.9}Mn_{0.1}O_5$, *Icmm*, synthesized in argon, as function of temperature. The magnetic transition temperature $T_N = 636(2)$ K.

Jahn–Teller distortion occurs at Mn sites which could weaken the superexchange.

Magnetic properties of air synthesized M = Co

The Co-compound, $Sr_2Fe_{1.9}Co_{0.1}O_{5.5}$, is isostructural with $Sr_4Fe_4O_{11}$ ($Sr_2Fe_2O_{5.5}$).[6] There is only a 5% substitution of Co for Fe and, thus, one might expect similar magnetic behavior. Magnetic susceptibility data for $Sr_2Fe_{1.9}Co_{0.1}O_{5.5}$ are shown in Fig. 15b–c. A FC/ZFC divergence occurs near ~230 K which can be taken as the magnetic transition temperature, T_N, which is

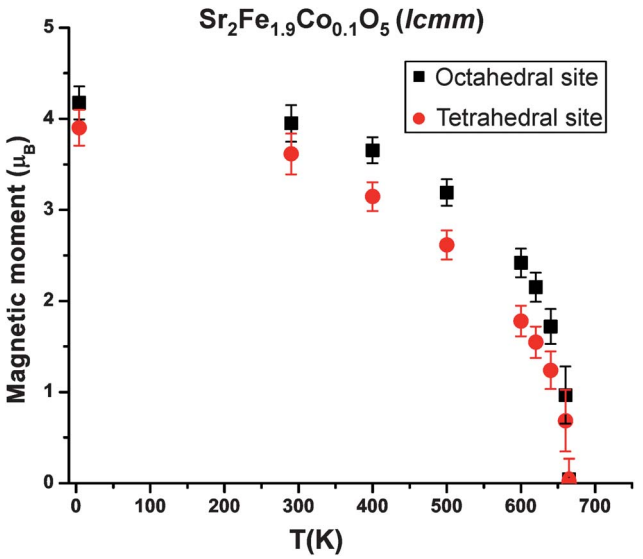

Fig. 14 The magnetic moments of $Sr_2Fe_{1.9}Co_{0.1}O_5$, *Icmm*, synthesized in argon, as function of temperature. The magnetic transition temperature $T_N = 663$ K.

very near the value for un-doped $Sr_4Fe_4O_{11}$ of 232 K.[24] A second anomaly is found below ~60 K in both the ZFC and FC data which has the appearance of spin freezing. No such feature is reported for $Sr_4Fe_4O_{11}$. The susceptibility above room temperature to 700 K is shown in Fig. 15c,d. The high temperature inverse susceptibility data, Fig. 15d, shows apparent Curie–Weiss behavior up to ~600 K, beyond which deviations set in. It is worth noting that neither of the other two oxidized phases, $Sr_2Fe_{1.9}M_{0.1}O_{5.5}$ M = Cr or Mn, show a Curie–Weiss regime up to 700 K nor do the related materials Sr_2FeMnO_{5+y}, y = 0.0, 0.5.[28] Nonetheless, a Curie–Weiss fit $\{\chi = C/(T - \theta)\}$ to the data between 300 K and 600 K yields C = 5.54(1) emu K mol^{-1} and $\theta = -75(1)$K. The measured C is less than the expected sum of contributions from high spin Fe^{3+} and Fe^{4+}(at this y-value equal concentrations are expected) of 7.38 emu K mol^{-1}. This could imply a moment reduction for one of the ions due to the square pyramidal geometry, perhaps. A more detailed discussion is rendered difficult due to a lack of consensus regarding either the extent of Fe^{3+}/Fe^{4+}charge ordering and the site preferences of the two ions.[6,24–27] A Curie–Weiss behavior is also reported for $Sr_4Fe_4O_{11}$ above 232 K,[24] but the data are not shown and no Curie constant is reported. However, $\theta = +598(9)$K, which is in profound disagreement with the value determined for the 5% Co doped material. In addition, the FC susceptibility is suggested to saturate at 5 K for $Sr_4Fe_4O_{11}$, while for $Sr_2Fe_{1.9}Co_{0.1}O_{5.5}$, saturation does not occur down to 5 K. $Sr_2Fe_{1.9}Co_{0.1}O_{5.5}$ shows clear hysteresis in isothermal magnetization data at 5 K and 100 K. The hysteresis at 5 K shows a residual moment of 0.0084 μ_B. This may indicate spin canting. Thus, there are significant differences in bulk magnetic properties between $Sr_2Fe_2O_{5.5}$ ($Sr_4Fe_4O_{11}$) and the phase studied here with 5% Co doping.

Neutron diffraction experiments were carried out at 4 K and 290 K. The difference plot, Fig. 16, shows the presence of many magnetic reflections, confirming long-range magnetic ordering, which can be indexed on the chemical cell as indicated.

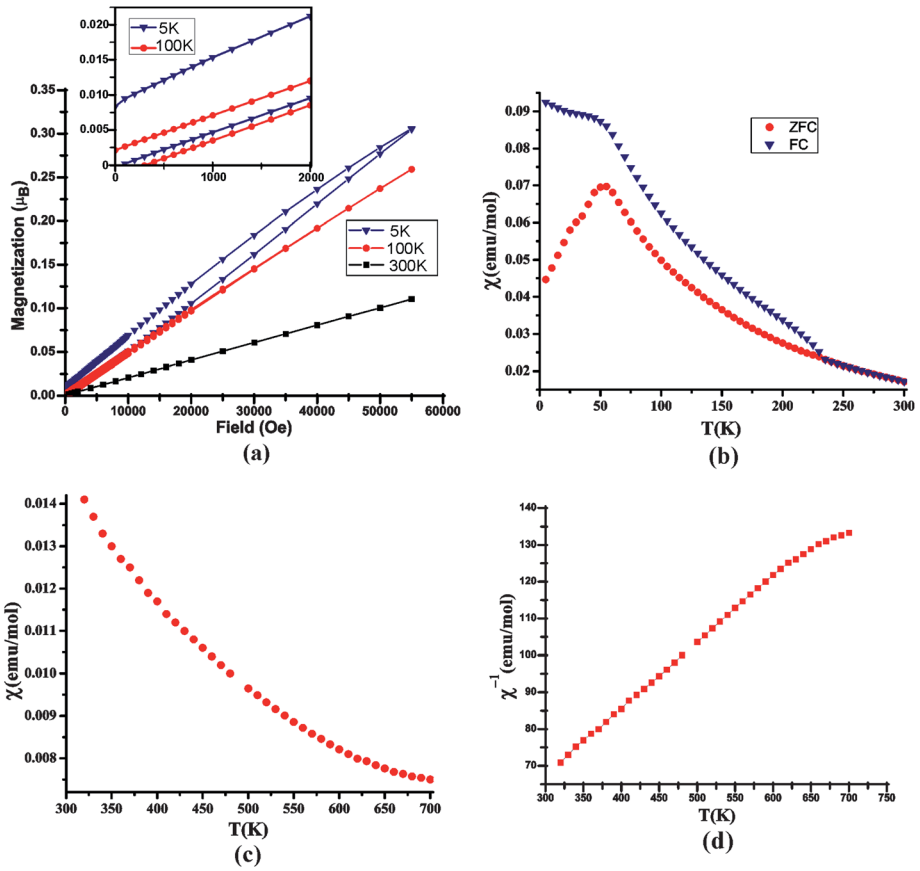

Fig. 15 Bulk magnetic data for $Sr_2Fe_{1.9}Co_{0.1}O_{5.5}$, *Cmmm*, synthesized in air. **(a)** Isothermal magnetization data. A hysteresis, magnified in the inset, occurs at 5 K, with a residual moment of 0.0084 μ_B. A smaller hysteresis is also present at 100 K. **(b)** Zero field cooled-field cooled (ZFC-FC) data from 5 K to 300 K. The FC data begins diverging from ZFC above ~230 K, which may indicate the transition to long range magnetic order. **(c)** Susceptibility data obtained while heating the sample from 300 K to 700 K. **(d)** Inverse susceptibility data from 300 K to 700 K. Deviation from the Curie-Weiss regime is evident in this figure.

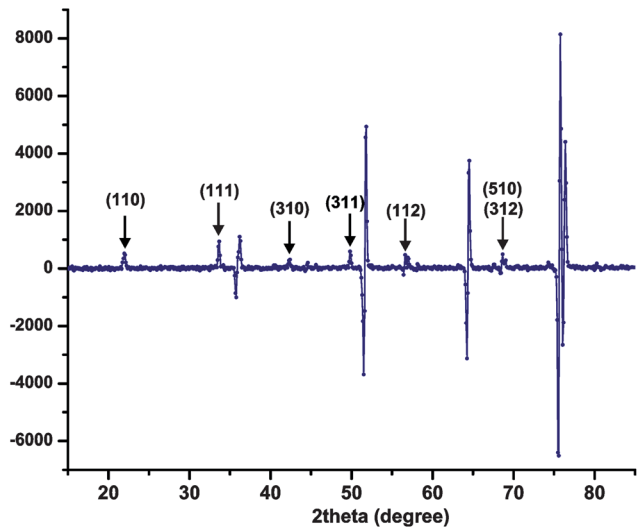

Fig. 16 The difference plot for $Sr_2Fe_{1.9}Co_{0.1}O_{5.5}$, *Cmmm*, obtained by subtraction of neutron data at 290 K from the data at 4 K. The indexes for the main magnetic peaks are shown. The valleys and their adjacent peaks are due to the small shift of structural peak positions in the 290 K data relative to the 4 K data.

Comparing with data for $Sr_4Fe_4O_{11}$[24] the magnetic diffraction patterns appear to be nearly identical. To summarize the situation for $Sr_4Fe_4O_{11}$, there are actually two proposed structural and magnetic structural models.[6,24] In both, the Fe^{3+} and Fe^{4+} ions site order on the square pyramidal and octahedral sites, but the site preferences are opposite. Several arguments have been presented for each site order preference but the issue appears to be still unresolved.[25–27] In any case the magnetic structure is C-type antiferromagnetic order on only one of the sites – the other remains non-magnetic to 4 K, due to local frustration. For example cations on the octahedral sites couple to four nearest square pyramidal neighbors and given AF order on these near neighbor sites, the frustration emerges. For $Sr_2Fe_{1.9}Co_{0.1}O_{5.5}$ several magnetic structure simulations and refinements were performed by the FullProf program suite,[17,18] using WinPLOTR.[18,19] As anticipated, an antiferromagnetic C-type model fits the data very well. The refinement profile and the magnetic structure are shown in Fig. 17 and 18. As seen in Fig. 18, the magnetic moments are oriented along the *b*-axis. As mentioned, only one of the two Fe sites is ordered, and Rietveld refinements give equally good results for both site preference choices, as observed for $Sr_4Fe_4O_{11}$.[24] The saturation magnetic moment obtained for $Sr_4Fe_4O_{11}$ at 1.5 K is 3.55(5) μ_B, unusually small

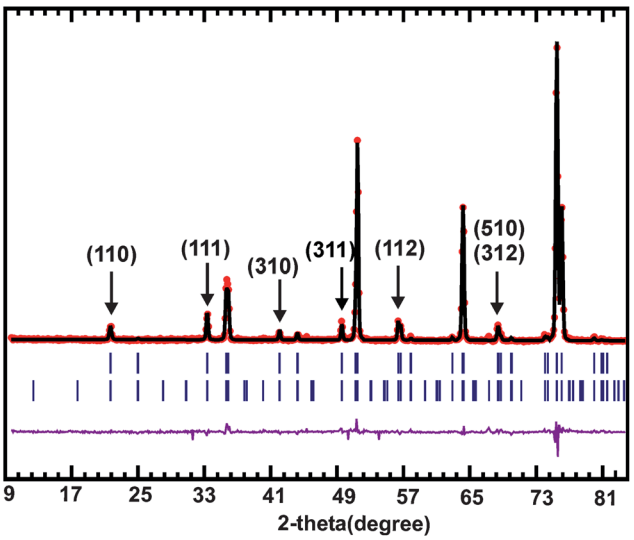

Fig. 17 The refinement profile for crystal and magnetic structures of $Sr_2Fe_{1.9}Co_{0.1}O_{5.5}$, *Cmmm*, synthesized in air. Only one of the two sites, square-pyramidal or octahedral sites, contributes to the C-type magnetic structure (Fig. 18). The Rietveld refinement gives equally good fits for both. Vertical tick marks show the positions of the peaks corresponding to the crystal (upper tick marks) and magnetic structures (lower tick marks). The purple solid line at the bottom is the difference plot.

for Fe^{3+} (S = 5/2), and was rationalized in terms of limited delocalization of d-electrons.[24] However, the refined moment for $Sr_2Fe_{1.9}Co_{0.1}O_{5.5}$ at 4 K is even smaller $\mu = 2.99\ (5)\ \mu_B$,

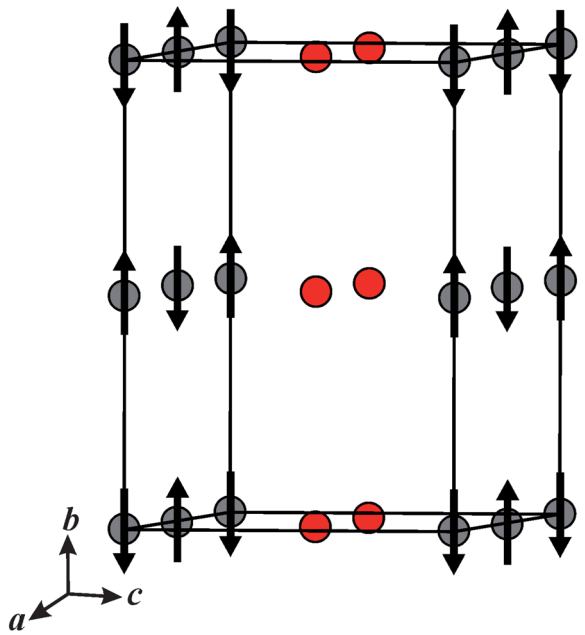

Fig. 18 The magnetic structure of $Sr_2Fe_{1.9}Co_{0.1}O_{5.5}$, *Cmmm*, synthesized in air, at 4 K. It is a C-type antiferromagnetic, and there are two competing models (1) Contribution to the magnetic structure from the octahedral sites only. (2) Contribution from the square-pyramidal sites only. The Rietveld refinement results are equally good for both models. The figure shows model number (2) with grey and red spheres representing square-pyramidal and octahedral sites, respectively.

which is a considerable difference, given the small degree of substitution. At present the origin of the moment reduction is unclear.

Magnetic properties of air synthesized M = Cr, Mn

For cubic $Sr_2Fe_{1.9}Cr_{0.1}O_{5+y}$ and $Sr_2Fe_{1.9}Mn_{0.1}O_{5+y}$ synthesized in air, bulk magnetic data are shown in Fig. 19 and 20. Both show FC/ZFC divergences, below ~60 K for the Cr and ~45 K for the Mn material. High temperature data indicate that a true Curie–Weiss paramagnetic regime is not achieved up to 700 K. Both also show hysteresis at 5 K with a residual moment of 0.0018 μ_B for the Cr-compound and of 0.0042 μ_B for the Mn-material. Such results might be indicative of a spin frozen ground state or an unusual superparamagnetic state as found for Sr_2FeMnO_5.[28]

Neutron diffraction data were obtained at 4 K and 300 K, shown in Fig. 21 and 22 for both compounds. The apparent absence of any intense magnetic Bragg peaks suggests that there is no long-range magnetic ordering in these two compounds down to 4 K. However, in both materials there exist complex features at 4 K that disappear at 300 K. The temperature dependence of these peaks indicates they are magnetic peaks, diagnostic of mostly short range magnetic interactions. The insets of Fig. 21 and 22 show these features. For the M = Mn phase there are two peaks at ~22 deg and ~33 deg which consist of a weak but sharp Bragg component superimposed on a broad diffuse peak. Fitting of the Bragg components gives precise positions of 21.83(3) deg and 33.45(3) deg which are apparently incommensurate with the *Pm*-3*m* unit cell but in fact index as (110) and (111) on the magnetic unit cell found for *Cmmm* $Sr_2Fe_{1.9}Co_{0.1}O_{5.5}$. This strongly suggests that the local chemical structure for the M = Mn phase is *Cmmm*-like in accord with the structural analysis presented in an earlier section. Underlying the Bragg peaks are very broad, diffuse peaks centered at the same positions, within error. Analysis of these peaks using the Ornstein-Zernike model[29] (Fig. 23) yields correlation lengths of 10(1) Å and 12(5) Å for the two peaks which agree within error. The fraction of the Bragg component to the total intensity is estimated as 0.08(2).

For the M = Cr material, only one such feature is seen, but now with the Bragg position at 30.69(3) deg indexes as (1/2 1/2 1/2) on the *Pm*-3*m* cell, *i.e.*, indicative of a G-type magnetic order. However, this position is very near those found for the pair of magnetic reflections, (101) and (011) observed for the *Icmm* $Sr_2Fe_{1.9}Cr_{0.1}O_{5.0}$ phase. Thus, it is more difficult to infer the average chemical structure from the magnetic scattering in this case. The diffuse component, analyzed in the same manner as described above gives a correlation length of 7(1) Å. As this is a much weaker feature, the Bragg/diffuse ratio is somewhat poorly defined. Nonetheless, based on these results one can rule out a random, spin frozen ground state for these two phases. The anomalies in the susceptibility may be better ascribed to an unusual superparamagnetic ground state. Thus, while the argon synthesized $Sr_2Fe_{1.9}M_{0.1}O_{5.0}$ phases show the expected magnetic structures, the three air synthesized materials are all different. Such a variation is remarkable given the low doping level of 5%.

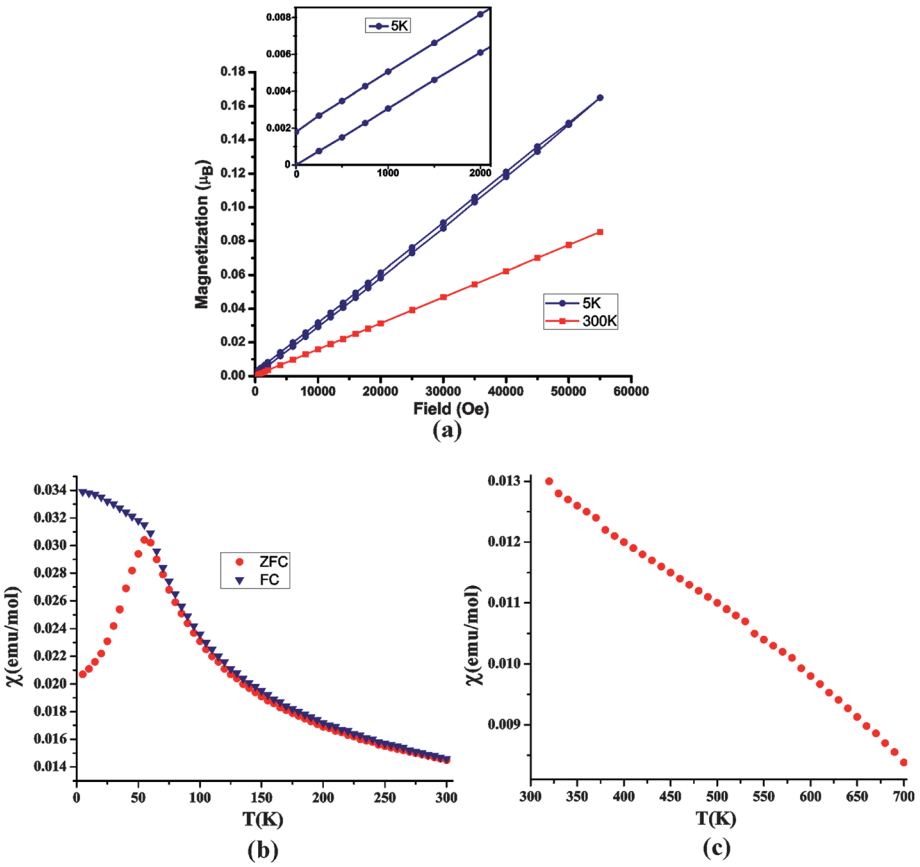

Fig. 19 Bulk magnetic data for $Sr_2Fe_{1.9}Cr_{0.1}O_{5+y}$, *Pm*-3*m*, synthesized in air. **(a)** Isothermal magnetization data at 5 K and 300 K. A hysteresis, magnified in the inset, occurs at 5 K, with a residual moment of 0.0018 μ_B. **(b)** Zero field cooled-field cooled (ZFC-FC) data from 5 K to 300 K. Note the divergence between ZFC and FC data below ~60 K, indicative of a possible spin-glass transition. **(c)** Susceptibility data obtained while heating the sample from 300 K to 700 K. As seen here the paramagnetic behavior does not occur up to 700 K.

Summary and conclusions

$Sr_2Fe_{1.9}M_{0.1}O_{5+y}$ (M = Mn, Cr, Co; y= 0, 0.5) were synthesized in air, y ~ 0.5, and argon, y ~ 0. The Ar-synthesized materials have long-range brownmillerite-type ordering of vacancies with long-range G-type magnetic ordering, and T_N = 652(2) K, 633(2) K, and 663(2) K, for the Cr, Mn and Co compounds, respectively. The low T_N for the Mn-compound can be due to the competing ferromagnetic interactions.

The air-synthesized Co-material is isostructural with *Cmmm* $Sr_2Fe_2O_{5.5}$ ($Sr_4Fe_4O_{11}$) with long-range vacancy ordering resulting in chains of corner-sharing octahedra separated by dimers of square-pyramids and a long-range C-type antiferromagnetic ordering with T_N ~ 230 K. The local structure is also well described by the *Cmmm* model. The air-synthesized Cr-material has a vacancy-disordered cubic structure. The M = Mn phase appears cubic but closer inspection shows a more complex picture with a likely core (*Pm*-3*m*)/shell (*Cmmm*) composite structure. The local structure of the M = Cr phase shows a *Cmmm* type ordering of oxygen vacancies. Neither the M = Cr or Mn phases show long-range magnetic order but short range correlations are evident from the weak peaks which develop in the neutron diffraction data upon cooling to 4 K. In both cases the peaks consist of a dominant, diffuse feature with a minor Bragg component. For the Mn-compound these peaks can be indexed as (110) and (111) on the C-type magnetic unit cell found for the M = Co phase, indicating the presence of C-type domains with correlation lengths of ~10(1) Å. For the Cr-compound the peak indexes as (1/2 1/2 1/2) on the *Pm*-3*m* cell indicative of short range G-type ordering with the correlation length 7(1) Å. These results rule out a random, spin frozen ground state for these two phases and suggest an unusual superparamagnetic state as found for Sr_2FeMnO_5.[28]

Acknowledgements

J.E.G. acknowledges the support of the Natural Sciences and Engineering Research Council (NSERC) of Canada through Discovery Grants. The authors thank Frank Gibbs for his help with the TGA measurements. This work has benefited from the use of NPDF at the Lujan Center at Los Alamos Neutron Science Center, funded by DOE Office of Basic Energy Sciences. Los Alamos National Laboratory is operated by Los Alamos National Security LLC under DOE Contract DE-AC52-06NA25396. The upgrade of NPDF has been funded by NSF through grant DMR 00-76488. The Canadian Neutron Beam Centre is funded jointly by NSERC and the National Research Council (NRC) of Canada. The work at the High Flux Isotope

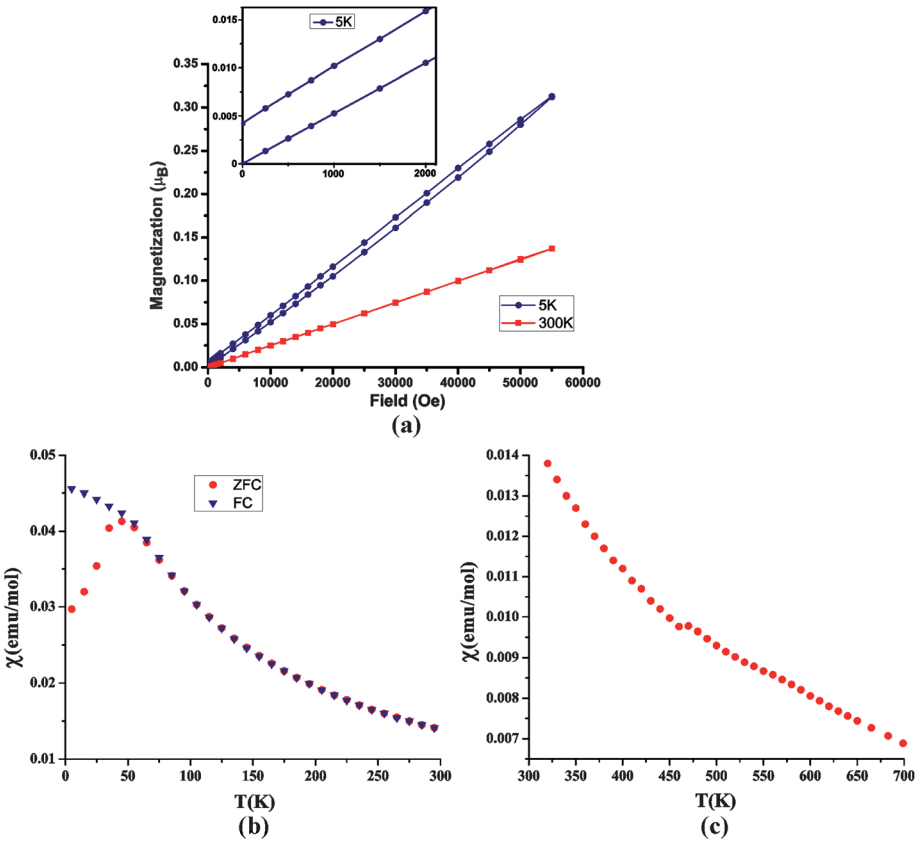

Fig. 20 Bulk magnetic data for $Sr_2Fe_{1.9}Mn_{0.1}O_{5+y}$, *Pm*-3*m*, synthesized in air. **(a)** Isothermal magnetization data. A hysteresis, magnified in the inset, occurs at 5 K, with a residual moment of 0.0042 μ_B. **(b)** Zero field cooled-field cooled (ZFC-FC) data from 5 K to 300 K. The divergence between ZFC and FC data happens below ~45 K. **(c)** Susceptibility data obtained while heating the sample from 300 K to 700 K. The paramagnetic regime is not achieved up to 700 K.

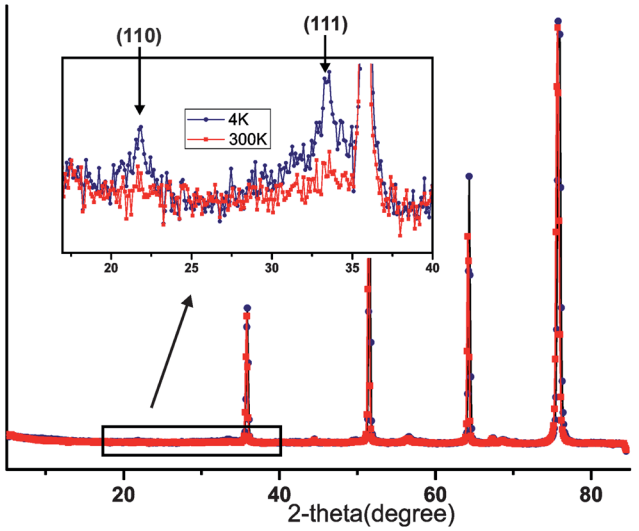

Fig. 21 The neutron diffraction data for $Sr_2Fe_{1.9}Mn_{0.1}O_{5+y}$, synthesized in air, at 4 K and 300 K. The diffuse temperature dependent peaks at 21.83(3)° and 33.45(3)°, highlighted in the inset, indicate the presence of short range magnetic interactions at low temperature. The peak positions can be indexed on the magnetic *Cmmm* unit cell (Fig. 18). The upper blue and the lower red patterns are the data at 4 K and 300 K, respectively.

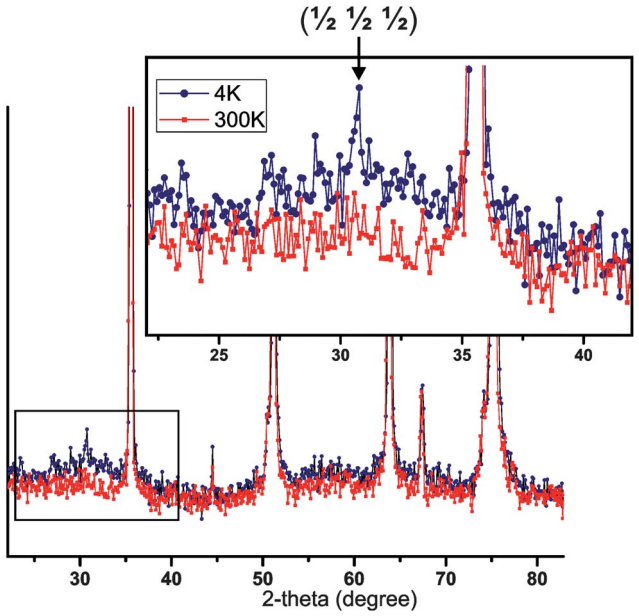

Fig. 22 The neutron diffraction data for $Sr_2Fe_{1.9}Cr_{0.1}O_{5+y}$, synthesized in air, at 4 K and 300 K. The diffuse temperature dependent peak at 30.69(3)°, highlighted in the inset, indicates the presence of short range G-type magnetic interactions at low temperature. The peak can be indexed on the *Pm*-3*m* cell. The upper blue and the lower red patterns are the data at 4 K and 300 K, respectively.

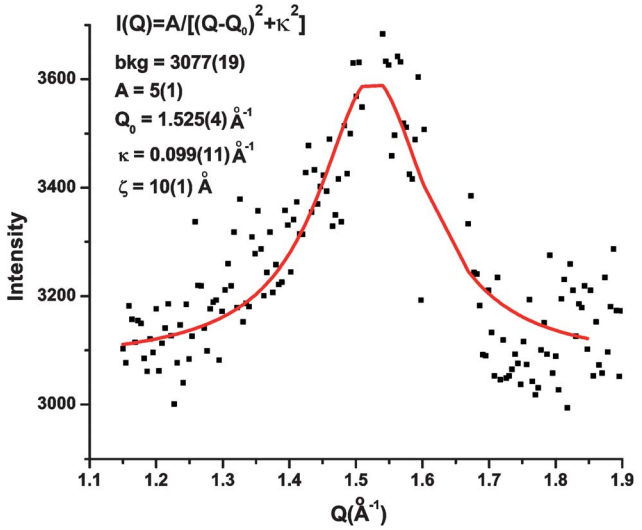

Fig. 23 The fit of the diffuse magnetic peak underlying the (111) magnetic Bragg peak (which has been removed) of $Sr_2Fe_{1.9}Mn_{0.1}O_{5+y}$ to the Ornstein-Zernike model, $I(Q) = A/[(Q - Q_0)^2 + \kappa^2]$ where $Q = 4\pi\sin\theta/\lambda$, A is an amplitude, Q_0 is the peak centre and $\kappa = 1/\xi$ with ξ being the correlation length.

Reactor, Oak Ridge National Laboratory (ORNL), was sponsored by the Scientific User Facilities Division, Office of Basic Energy Sciences, U.S. Department of Energy (U.S. DOE). ORNL is operated by UT Battelle, LLC for the U.S. DOE under Contract No. DEAC05-00OR22725.

References

1 J. Sunarso, J. Motuzas, S. Liu and J. C. D. d. Costa, *J. Membr. Sci.*, 2010, **361**, 120–125.
2 T. Kida, A. Yamasaki, K. Watanabe, N. Yamazoe and K. Shimanoe, *J. Solid State Chem.*, 2010, **183**, 2426–2431.
3 Z. Gong, X. Yin and L. Hong, *Solid State Ionics*, 2009, **180**, 1471–1477.
4 G. Zhang, X. Dong, Z. Liu, W. Zhou, Z. Shao and W. Jin, *J. Power Sources*, 2010, **195**, 3386–3393.
5 J. Richter, P. Holtappels, T. Graule, T. Nakamura and L. Gauckler, *Materials design for perovskite SOFC cathodes*, Springer Wien, 2009.
6 J. P. Hodges, S. Short, J. D. Jorgensen, X. Xiong, B. Dabrowski, S. M. Mini and C. W. Kimball, *J. Solid State Chem.*, 2000, **151**, 190–209.
7 V. Garlea, B. Chakoumakos, S. Moore, G. Taylor, T. Chae, R. Maples, R. Riedel, G. Lynn and D. Selby, *Appl. Phys. A: Mater. Sci. Process.*, 2010, **99**, 531–535.
8 T. Proffen, T. Egami, S. J. L. Billinge, A. K. Cheetham, D. Louca and J. B. Parise, *Appl. Phys. A: Mater. Sci. Process.*, 2002, **74**, s163–s165.
9 A. C. Larson and R. B. Von Dreele, *General Structure Analysis System (GSAS), Los Alamos National Laboratory Report LAUR*, 1994, pp. 86–748.
10 B. H. Toby, *J. Appl. Crystallogr.*, 2001, **34**, 210–213.
11 F. Ramezanipour, J. E. Greedan, A. P. Grosvenor, J. F. Britten, L. M. D. Cranswick and V. O. Garlea, *Chem. Mater.*, 2010, **22**, 6008–6020.
12 T. G. Parsons, H. D'Hondt, J. Hadermann and M. A. Hayward, *Chem. Mater.*, 2009, **21**, 5527–5538.
13 F. Ramezanipour, B. Cowie, S. Derakhshan, J. E. Greedan and L. M. D. Cranswick, *J. Solid State Chem.*, 2009, **182**, 153–159.
14 P. D. Battle, S. K. Bollen, T. C. Gibb and M. Matsuo, *J. Solid State Chem.*, 1991, **90**, 42–46.
15 C. L. Farrow, P. Juhás, J. W. Liu, D. Bryndin, E. S. Božin, J. Bloch, T. Proffen and S. J. L. Billinge, *J. Phys.: Condens. Matter*, 2007, **19**, 335219.
16 M. G. Tucker, D. A. Keen, M. T. Dove, A. L. Goodwin and Q. Hui, *J. Phys.: Condens. Matter*, 2007, **19**, 335218.
17 J. Rodríguez-Carvajal, *Physica B: Condensed Matter*, 1993, **192**, 55–69.
18 J. Rodriguez-Carvajal and T. Roisnel, *FullProf.98 and WinPLOTR: New Windows 95/NT Applications for Diffraction*, 1998.
19 T. Roisnel and J. Rodriguez-Carvajal, *WinPLOTR: a Windows tool for powder diffraction patterns analysis*, in *Proceedings of the Seventh European Powder Diffraction Conference (EPDIC 7), Materials Science Forum*, ed. R. Delhez and E.J. Mittenmeijer, 2000, pp. 118–123.
20 M. F. Collins, in *Magnetic Critical Scattering*, Oxford University Press, New York, Oxford, 1989, p. 29.
21 M. Schmidt and S. J. Campbell, *J. Solid State Chem.*, 2001, **156**, 292–304.
22 R. L. Martin, in *New Pathways in Inorganic Chemistry*, ed. E. A. V. Ebsworth, A. G.Maddock and A. G. Sharpe, Cambridge University Press, New York, 1968.
23 J. B. Goodenough, *Magnetism and the Chemical Bond*, Interscience, New York, 1963.
24 M. Schmidt, M. Hofmann and S. J. Campbell, *J. Phys.: Condens. Matter*, 2003, **15**, 8691–8701.
25 P. Ravindran, R. Vidya, H. Fjellvåg and A. Kjekshus, *Phys. Rev. B: Condens. Matter Mater. Phys.*, 2008, **77**, 134448.
26 P. Adler, *Phys. Rev. B: Condens. Matter Mater. Phys.*, 2008, **77**, 136401.
27 P. Ravindran, R. Vidya, H. Fjellvåg and A. Kjekshus, *Phys. Rev. B: Condens. Matter Mater. Phys.*, 2008, **77**, 136402.
28 F. Ramezanipour, J. E. Greedan, J. Siewenie, T. Proffen, D. H. Ryan, A. P. Grosvenor and R. L. Donaberger, *Inorg. Chem.*, 2011, **50**, 7779–7791.
29 H. E. Stanley, *Introduction to Phase Transitions and Critical Phenomena*, Oxford Univ. Press, New York, 1971.

